

University of Nevada, Reno

# Quantum Dot Sensitized Nanotubes for Full Solar Spectrum Photovoltaic Cell

A THESIS SUBMITTED IN PARTIAL FULFILLMENT OF THE  
REQUIREMENTS FOR THE DEGREE OF MASTER OF SCIENCE IN

Materials Science and Engineering

by

Sohana Khanal

Dr. Manoranjan Misra / Thesis Advisor

December, 2010



THE GRADUATE SCHOOL

We recommend that the thesis  
prepared under our supervision by

**SOHANA KHANAL**

entitled

**Quantum Dot Sensitized Nanotubes for Full Solar Spectrum Photovoltaic Cell**

be accepted in partial fulfillment of the  
requirements for the degree of

**MASTER OF SCIENCE**

Manoranjan Misra, Ph.D., Advisor

Krishnan Raja, Ph.D., Committee Member

Carl Nesbitt, Ph.D., Graduate School Representative

Marsha H. Read, Ph. D., Associate Dean, Graduate School

December, 2010

## ABSTRACT

The demand for energy with limited non-renewable sources of energy has called researchers to find clean renewable energy sources. Solar light is considered good choice of the alternate energy. Our effort in this work was to investigate efficient photovoltaic (PV) systems by designing a hybrid photoelectrode with good absorption as well as charge transport properties. A coupled semiconductor material, one-dimensional TiO<sub>2</sub> nanotubes (1D TiO<sub>2</sub>-NTs), filled with low band semiconductor quantum dots (QDs), PbS QDs, for better charge carrier transport was prepared and investigated. The vertically standing self assembled nanotubular array was attained by anodizing the Ti metal in two different solutions: 1) Ethylene Glycol with 0.5 wt% NH<sub>4</sub>F and 3 vol percent water and 2) 0.5M H<sub>3</sub>PO<sub>4</sub> with 0.5 wt% NH<sub>4</sub>F. The anodized samples were annealed and then filled with the nanoparticles of other low band gap semiconductor materials. The CdS nanoparticles were used for the better understanding of the sensitizing process. The material was then switched to the PbS. As in the hypothesis, if PbS quantum dots are uniformly distributed in the 1D TiO<sub>2</sub> Multiple Charge Carrier Generation can be created since PbS has a small band gap. A chemical bath deposition process in the presence of ultrasonic waves was adopted for the deposition of the QDs. Saturated lead sulfide solution was used as the lead source and the 0.2 M Na<sub>2</sub>S solution for the sulfur source. The process resulted in the successful uniform deposition of the PbS QDs onto the 1D TiO<sub>2</sub> NTs. The deposited compound obeyed the stoichiometric ratio of 1:1 as desired. Photocurrent densities of 4.5 mA/cm<sup>2</sup> was obtained, which is higher than the TiO<sub>2</sub> alone in a polysulfide solution. PbS-TiO<sub>2</sub> can be a suitable candidate for harvesting a broad solar spectrum as the UV-vis study proved that they absorb the light in the UV range.

## ACKNOWLEDGEMENTS

First and foremost I extend my sincere appreciation and gratitude to my advisor, Dr Mano Misra, for his advice, inspiration, encouragement and faith in me. This thesis would not have been possible without Dr. Misra's constant support and faith. Working with Dr. Misra and his research group gave me the opportunity to build up as a researcher as well as a strong person.

I would also like to thank Dr. Krishnan Selva Raja for the constant support throughout my Masters journey. Dr. Raja was available whenever I needed his advice on anything. He was always ready with the detailed information and instruction about the project. His patience and guidance towards his students is very motivating.

I would also like to take this opportunity to thank Dr. Carl C. Nesbitt for accepting to serve in my thesis committee. I would also like to thank Dr. Gautam Priyadarshan for helping me with the SEM. I am grateful for the support from the Department of Chemical and Metallurgical Engineering. I would also like to thank my group members for their support and friendship which made my time at research lab wonderful.

I am indebted to my parents who encouraged me throughout my life in whatever I do. Being half a globe apart from the family is not easy. But with the help and support from my friends, colleagues and professors at UNR, this journey was much easier.

## TABLE OF CONTENTS

<b>1 Introduction</b>	<b>1</b>
1.1 Background .....	1
1.2 Solar-cell basics .....	4
1.2.1 Semiconductor Concepts .....	4
1.2.2 Application of Semiconductors .....	11
1.2.3 Photoelectrochemical cells .....	18
1.3 Working Principles of Solar Cells .....	20
1.4 Development in PV Cells .....	23
1.5 Types of Solar Cells .....	24
1.6 Dye-Sensitized Solar Cells .....	26
1.7 Quantum Dot Solar Cells .....	28
<b>2 Materials and Methods</b>	<b>34</b>
2.1 Materials and Chemicals required .....	34
2.2 Synthesis Procedure .....	34
2.2.1 Preparation of TiO <sub>2</sub> .....	34
2.2.2 Introduction of QDs into TiO <sub>2</sub> .....	36
<b>3 Characterization Techniques</b>	<b>41</b>
3.1 Scanning Electron Microscope .....	41
3.2 Transmission Electron Microscope .....	41
3.3 UV-Vis Measurement .....	42
3.4 Photochemical Measurements .....	42
3.5 Corrosion Potential .....	43
3.6 Impedance and Mott-Schottky Measurements .....	44
3.7 Photovoltaic Study .....	45
<b>4 Result and Discussion</b>	<b>47</b>

4.1 TiO <sub>2</sub> Nanotubes .....	47
4.2 CdS introduced TiO <sub>2</sub> Nanotubes .....	49
4.2.1 Morphological Study .....	49
4.2.2 UV-Vis study .....	50
4.3 Studies performed on PbS sensitized TiO <sub>2</sub> nanotubes .....	52
4.3.1 Morphological Study .....	52
4.3.2 TEM (PbS-TiO <sub>2</sub> ) .....	61
4.3.3 DRUV-Vis Study .....	62
4.3.4 PEC studies (PbS-TiO <sub>2</sub> ) .....	66
4.3.5 Mott-Schottky Study .....	77
4.3.6 Electrochemical Impedance Analysis .....	82
4.3.7 Photovoltaic Study (PbS-TiO <sub>2</sub> ) .....	85
<b>5 Conclusion</b> .....	<b>88</b>
<b>References</b> .....	<b>89</b>

## List of Tables

- 4.1: Band gap comparison of DRUV-Vis data of TiO<sub>2</sub> NTs, CdSNP-TiO<sub>2</sub>NT and CdSQD-TiO<sub>2</sub>NT with the PbSQD-TiO<sub>2</sub>NTs annealed and as prepared samples

## List of Figures

### Chapter 1

- 1.1: Historical and Projected energy consumption in the world
- 1.2: Schematic illustration of typical band diagrams for metals, semiconductors (at T=0K) and insulators. Dash line represents the Fermi level (explained below). Darker region represents the filled band, whereas the lighter region represents the empty band
- 1.3: Two step recombination process via a trapping level within the forbidden gap of a semiconductor
- 1.4: Hot carrier relaxation/cooling dynamics in semiconductors
- 1.5: Schematic representation of *p-n junction*: (a) energy level for p-type and n-type semiconductors, (b) energy level for the same material after they are brought together to create junction (in thermal equilibrium), and (c) p-n junction showing space-charge carrier (or depletion region)
- 1.6: Energy Band diagram at a metal-semiconductor heterojunction: a) at thermal equilibrium, b) at forward bias and c) at reverse bias. Where:  $\Phi_b$  is the height of the barrier, q is the electron charge
- 1.7: (a) Current component in Schottky diode in dark. (b) Comparison of the illuminated characteristics of Schottky and p-n junction devices

- 1.8: (a) typical sketch for a MIS semiconductor. 3-D Energy band diagram at the (b) equilibrium condition, (c) equilibrium condition under a gate bias and (d) equilibrium condition under both drain and gate bias
- 1.9: Schematic representation of quantum tunneling through a barrier
- 1.10: (a) Photon passes through—not enough energy to create an exciton (b) A photon with energy greater than the band gap energy—more than enough energy to create an excitons
- 1.11: The Current vs Voltage plot for an ideal solar cell under both illuminated and dark conditions. In the graph,  $\eta$  is the efficiency of the solar cell.
- 1.12: Evolution of PV technology: from Silicon based solar cell to nanostructured solar cells
- 1.13: Structure of solid-state dye-sensitized nanocrystalline TiO<sub>2</sub> solar cells
- 1.14: Photovoltaic efficiency enhancement for the quantum dot solar cell via impact ionization

## **Chapter 2**

- 2.1: Schematic representation for the Anodization set-up for Ti foil
- 2.2: The set-up for the reflux process: a triple neck round bottom flask connected with the condenser

## **Chapter 3**

## **Chapter 4**

- 4.1: Top surface view of the nanotubular oxide layer on the Ti foil after anodizing in ethylene glycol solution. The diameter of the nanotubes were between the range of 60-80 nm

- 4.2: Top Surface morphology of the nanotubular oxide layer formed on the Ti foil after anodization in acidic solution. Self organized array of nanotubes with the diameter in the range of 70-90 nm. The nanotubes formed in acidic solution were a little wider than that formed in the organic solution
- 4.3: SEM image of as-prepared CdS-TiO<sub>2</sub> (a) side view for the composite prepared (b) top surface view for the CdS-TiO<sub>2</sub> as prepared. (c) Elemental analysis for CdS-TiO<sub>2</sub> confirming the presence of Cd and S at the ratio of almost 1:1. The SEM images show that the particles size are larger than intended but the elemental analysis prove that the materials still follow the required stoichiometric ratio
- 4.4: DRUV-vis spectra of annealed TiO<sub>2</sub> in comparison with CdS-TiO<sub>2</sub> NPs and CdS QDs
- 4.5: PbS nanoparticles formed after the reflux process
- 4.6: EDX analysis for the PbS-TiO<sub>2</sub> prepared via reflux process
- 4.7: Morphology of PbS nanoparticles deposited in the TiO<sub>2</sub> nanotubes (a) QDs obtained after three SILAR cycles with less coverage, (b) The QDs being deposited inside the TiO<sub>2</sub> NTs, (c) PbS QDs onto TiO<sub>2</sub> NTs by a SILAR method where the uniformly distributed particles have a surface coverage of about 30-40%, and (d) PbS QDs of size less than 10 nm was obtained
- 4.8: EDX analysis shows the presence of Pb and S for the PbS-TiO<sub>2</sub> NTs as prepared via chemical bath deposition
- 4.9: (a) and (b): HRTEM images for PbS deposited onto TiO<sub>2</sub>
- 4.10: DRUV-vis of the TiO<sub>2</sub>, PbS-TiO<sub>2</sub> NPs composite
- 4.11: DRUV-vis of the TiO<sub>2</sub>, PbS-TiO<sub>2</sub> NPs, 6 cycles of chemical deposition and 9 cycles of chemical deposition resulted in various particle size range which showed in the difference in the on-set absorbance

- 4.12: DRUV-vis spectra of the  $\text{TiO}_2$ ,  $\text{TiO}_2$ -PbS in comparison with the  $\text{TiO}_2$ -PbS annealed vs. the as prepared samples
- 4.13: Open Circuit Potential plots with and without illumination (a)  $\text{TiO}_2$  nanotubes prepared by anodization of Ti in  $\text{H}_3\text{PO}_4$  with M NaF solution; (b) PbS- $\text{TiO}_2$  composite as prepared.
- 4.14: Comparison between the annealed and non annealed PbS- $\text{TiO}_2$  samples to study the Open Circuit Potential plots with and without illumination. The annealed samples were annealed in inert Argon atmosphere at 200 °C for 2 h.
- 4.15: Photocurrent generation characteristic of PbS- $\text{TiO}_2$  NTs as a function of applied potential in the polysulfide electrolyte under AM 1.5 light illumination. (a)  $\text{TiO}_2$  nanotubes prepared by anodization of Ti in  $\text{H}_3\text{PO}_4$  with NaF solution; and (b) PbS- $\text{TiO}_2$  composite as prepared. The nanotubes were annealed in inert Argon atmosphere at 200 °C for 2 h.
- 4.16: Long-term photocurrent stability (current vs time) study of the materials transient behavior of (a) acid anodized  $\text{TiO}_2$ ; and (b) prepared composite  $\text{TiO}_2$ -PbS. The photon source was applied by AM 1.5 light in polysulfide electrolyte.
- 4.17: Mott-Schottky plots for the annealed  $\text{TiO}_2$  samples with and without illumination: (a) Acid anodized sample; and (b) Ethylene Glycol anodized samples.
- 4.18: Mott-Schottky plots of the PbS- $\text{TiO}_2$  with and without illumination: (a) PbS sensitized in acid anodized  $\text{TiO}_2$ ; and (b) PbS sensitized in Ethylene Glycol anodized  $\text{TiO}_2$ .
- 4.19: Complex plane electrochemical impedance behavior of the materials: a)  $\text{TiO}_2$  prepared in acid solution and b)  $\text{TiO}_2$  prepared in ethylene glycol based solution
- 4.20: Complex plane electrochemical impedance behavior of the materials: PbS QDs sensitized  $\text{TiO}_2$  nanotubes

4.21: Characteristic of PbS-TiO<sub>2</sub> nanotubular photovoltaic cell with Na<sub>2</sub>S/Na<sub>2</sub>S<sub>2</sub>O<sub>3</sub> electrolyte system with illumination of simulated solar light

## Chapter 1: Introduction

### 1.1 Background

Human population has been increasing rapidly which also increases the need of basic necessities like food, water, and most importantly, energy. Energy has been the fundamental requirement for civilization for centuries. The demand for energy is increasing daily with the increase in population but the supply is limited if we do not have renewable sources of energy. The modern society of industrialization consumes energy at a very high rate which decreases the supply of fossil fuel [1]. The continuous increase in world population directly affects the energy consumption. Especially in developing countries, as they attempt to improve their living standards [2]. The Energy Information Agency (EIA), U.S. Department of Energy projects the energy consumption of the world by the end of the year 2030 (Figure 1.1).

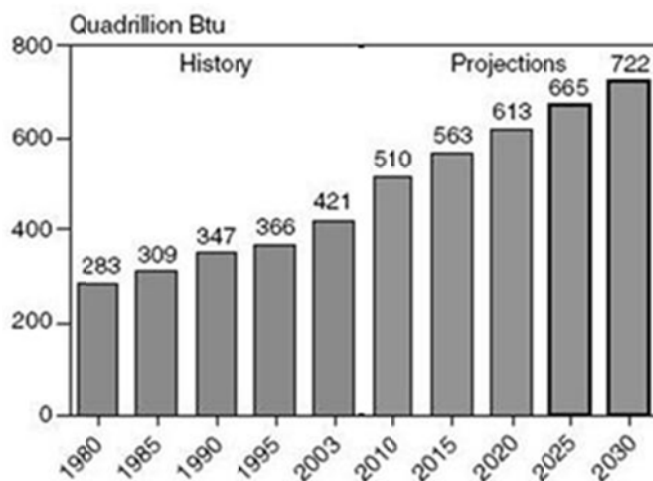


Figure 1.1: Historical and Projected energy consumption in the world [1]

International Energy Agency (IEA) France released the data showing that today the largest source for the electricity is coal [3]. The increase in demand of energy and diminishing of the non-renewable sources has motivated the scientists all over the world to find innovative alternative energy sources. At present the main source of the energy supply is fossil fuel. There needs to be a remarkable change in the energy source as the reserves are decreasing with daily use and the increasing demand for energy while there have been investigation for renewable source for energy, a key factor of 'clean energy' enters the picture. The concentration of greenhouse gas, particularly CO<sub>2</sub>, has risen to 360 ppm (parts per million) [4] since the late 19<sup>th</sup> century. With respect to the current consumption rate and demand of the fossil fuel, the CO<sub>2</sub> concentration is predicted to raise as high as 750 ppm by 2010 [5]. With this scenario the planet earth will be a less inhabitable place to live. Therefore search of the source for renewable clean energy has been essential. Lewis [5] in his presentations argues that among all the other alternative energy resources, like biomass, hydro, geothermal and wind power; solar cells have the strong potential to face this demand. But first we need to understand that unlike coal, the energy is not produced by solar cells itself, but it is converted. Solar cells take in the sunlight and convert it into the electrical energy. In our study, we focus upon the PV (photovoltaic) cell. A PV cell or a solar cell is the smallest building block of a photovoltaic system.

By definition [6]:

***Solar Cells:** a photovoltaic cell that converts sunlight directly into electricity*

***Quantum dot:** nanometer size semiconductor whose excitons are confined in all three spatial dimensions. They have the properties that are in between those of the bulk semiconductors and those discrete molecules.*

Derived from Greek, ‘photo’ means light and ‘voltaic’ means electricity. The conversion of the solar energy directly into electricity via semiconductor materials is the purpose of a Photovoltaic system, or commonly known as solar cells. The PV cell was first discovered by French physicist Edmond Becquerel as early as 1839. The technology has been part of our life for a very long time now. Although Becquerel discovered this process of using sunlight to produce electricity in a solid material in the early 19<sup>th</sup> century, it took more than a century for researchers all over the world to fully understand this process [7].

Eventually the progress was rapidly made on the technological aspect of the process. Gradually the studies proved that the photovoltaic effect caused certain materials to convert light energy into electrical energy at the atomic level [7-8]. The solar cells have been used in different products, such as calculators and wristwatches. More complex PV systems have also been incorporated in larger systems to provide power for communications satellites, water pumps, lights, appliances, and other machines. As of

today, various traffic signals are also powered by PV. In many cases, PV power is the least expensive form of electricity for these tasks.

Although solar energy is abundantly available there are few effective ways of using it for energy production. Storing this energy has been a major challenge as well. As of 2009 solar energy is used to supply only 0.04% of the total energy use [9]. The cost of energy produced under this process as estimated by the National Renewable energy laboratory in the year 2005 was around 11 to 15 cents/kWh [8].

Some important principles and properties of the semiconductors and solar cells are briefly discussed in this section to understand the concept better. Although this thesis article mostly focuses on the chemical synthesis and the characterization of the quantum dots incorporated in solar cells, it is very important to understand the basic principles behind the solar cell, so that materials with better photoactivity can be designed.

## **1.2 Solar-cell basics:**

### **1.2.1 Semiconductor Concepts:**

Semiconductors are the class of solid materials with the existence of a band gap. At  $T = 0$  K the gap is the energy difference between the valance (filled) band and the conduction (empty) band of the material (Figure 1.2). As the figure illustrates the semiconductor material differs from metals and insulators with respect to the band gap. This band gap (also referred as the energy gap),  $E_g$ , typically lies in the range between 0 and 4 eV for semiconductors. The most important and the distinctive property of the semiconductor is its temperature dependence of conductivity. Unlike metals, the

conductivity in the semiconductors increases with increasing temperature. Some common semiconductors that are widely used in the electronic and optoelectronic applications are Si, Ge, ZnS, CdS, PbS, CdTe, etc.

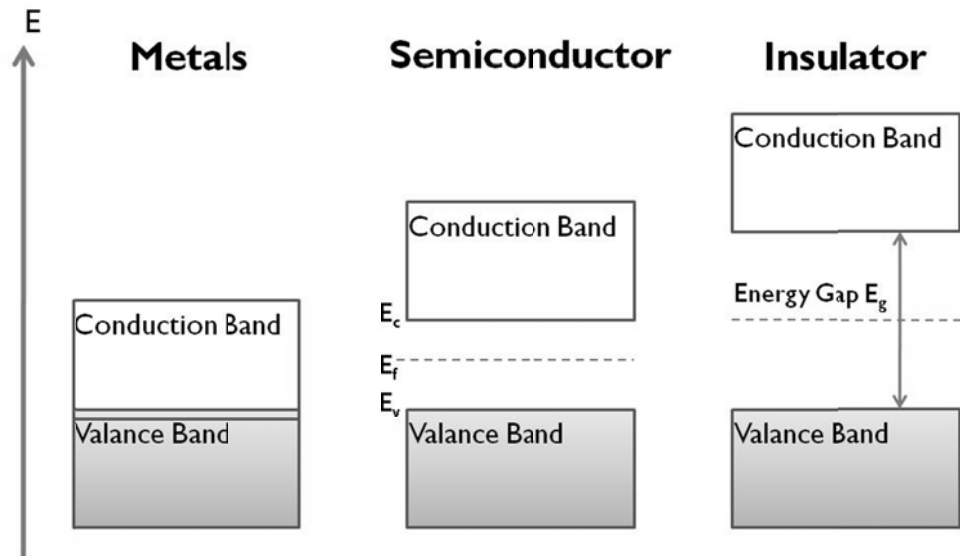


Figure 1.2: Schematic illustration of typical band diagrams for metals, semiconductors (at  $T=0K$ ) and insulators. Dash line represents the Fermi level (explained below). Darker region represents the filled band, whereas the lighter region represents the empty band [10].

In a semiconductors containing no defects, at  $T > 0K$ , some thermally excited electrons jump from the occupied valance band to the empty conduction band. The finite numbers of unoccupied states in the valance band are called *holes*, which may be regarded as the positive charge carrier contributing to the conduction process. The holes are nothing but the empty spaces left behind by the moving electrons. The generated holes and the negative charge carrier in the conduction band are together referred as the *electron-hole pairs*. These electrons and holes are the free charge carriers. The pairs can gain kinetic energy since the quasi-continuum of higher or lower states are available to

them, respectively. Therefore, in the presence of the electric field  $\epsilon$ , they respond and attain drift velocity  $v$ , and a net current density  $J$  [10-11].

During this process of forming the holes, in equilibrium, the concentration of electron ( $n$ , possess negative charge) in the conduction band is equal to the concentration of holes ( $p$ , possess positive charge) in the valance band the overall process can be expressed by,

$$n = p = n_i$$

where,  $n_i$  is the intrinsic carrier concentration.

The equilibrium concentrations of the charge carriers in semiconductors can be tailored by extrinsic dopants. The occupation statistics of the energy levels by the carriers is governed by the *Fermi-Dirac occupation statistics*,

$$F(E) = \frac{1}{1 + \exp\left(\frac{E - E_f}{kT}\right)}$$

Where, 'k' is the Boltzmann's constant and 'T' the absolute temperature. The energy function  $E_f$  is called the *Fermi Energy* or also known as *Fermi-Level*, which is defined as the energy level where the probability of being occupied by an electron is exactly  $\frac{1}{2}$  [12].

The semiconductors are classified into two main categories depending on the concentration of the majority carrier present: n-type and p-type. The n-type consists of electron and p-type consists of holes as their majority carriers. The Fermi-level for these can be calculated using following relations:

$$n = N_c \exp\left(-\frac{E_c - E_f}{kT}\right)$$

$$p = N_v \exp\left(-\frac{E_f - E_v}{kT}\right)$$

where,  $n$  and  $p$  are similar to the donor and acceptor density respectively.  $N_c$  and  $N_v$  are the effective densities of states in the conduction and valance band respectively. In equilibrium, the  $n$  and  $p$  can be described as,

$$np = n_i^2 = N_c \cdot N_v \cdot \exp\left(-\frac{E_g}{kT}\right)$$

where,  $E_g$  is the band gap of the material.

### **Non equilibrium properties of the carriers**

A semiconductor system is considered to be in non-equilibrium condition when the equation,  $n \cdot p = n_i^2$  is no longer satisfied. The conditions such as, under illumination or under carrier injection due to externally applied electric bias are the non-equilibrium factors. During this the fermi level is no longer uniform. In these conditions the carrier occupation can be described by introducing *quasi-Fermi levels*,  $E_{fn}$  and  $E_{fp}$  for electrons and holes respectively. The charge carrier densities with respect to the quasi-Fermi level are best described as,

$$n = N_c \exp\left(-\frac{E_c - E_{fn}}{kT}\right)$$

$$p = N_v \exp\left(-\frac{E_{fp} - E_v}{kT}\right)$$

At equilibrium,  $E_{fn} = E_{fp} = E_f$ . When the system is disturbed with dopants, the excess electron and hole injected in the semiconductor system moves the Fermi level towards the conduction band and valance band, respectively.

The non-equilibrium carrier properties provide an important characteristic of the material while considering the carrier recombination for device applications.

### **Interaction of light with Semiconductors**

When a monochromatic ray of incident light (I) hits the semiconductor, a certain amount (R) is refracted and certain fraction (T) is transmitted. The transmitted light is absorbed by the material, to excite the electrons. The light is the energy source for the electrons to jump from one energy state to the other. When the energy of the photons is greater than the energy gap of the semiconductor, the absorption in the material occurs to excite the electrons from the highly occupied valance band towards the empty conduction band [13-14].

Various excitations, such as, photon, electron irradiation, may lead to the generation of charge carriers.

### **Recombination Process:**

During illumination of the semiconductor with appropriate wavelength light, the electron-hole pairs are formed. This increases the concentration of the carriers in the illuminated state as compared to the dark state. Once the light is discontinued the charge carries decay back to the equilibrium values. The process of decaying is called recombination [10, 15]. The recombination process may occur in one of a few possible

ways: a) an electron gives up its energy through radiative recombination which involves emission of a photon, b) the electron loses energy through Auger recombination (i.e. transferring energy to another electron[16]), or c) phonon is generated hence losing the energy of an electron [15, 17].

The studies have shown that the defects in the semiconductors give rise to the energy levels within the otherwise forbidden gap. When this occurs, the recombination process is slowed down. As shown in Figure 1.3, the electron shifts from the conduction band to the so-called the defect energy level, then moves to the valence band, annihilating the hole. These are called traps.

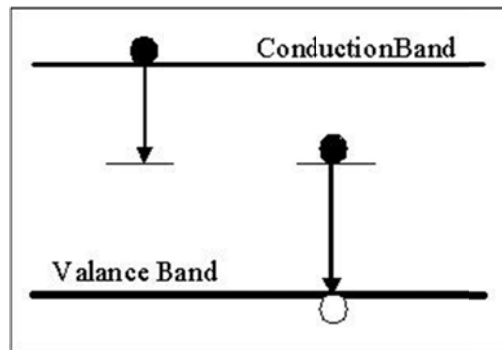


Figure 1.3: Two step recombination process via a trapping level within the forbidden gap of a semiconductor [17]

The system loses energy due to the recombination process. When the photon is discontinued and the recombination occurs, the flow of charge stops giving us zero current output. Therefore when we have external trap into the system, the recombination process is slowed down, allowing the charge to flow. As a result of this two step recombination process, we have higher chance of charge carrier moving around the

system. This particular behavior may bring down the efficiency of the cell. This challenge can be improved by combining the QDs with another appropriate semiconductor [18], in our case TiO<sub>2</sub> nanotubes.

### **Transport Process:**

The charge in solid is carried out by the motion of electrons throughout the delocalized band states in the solid. For the further understanding of the charge transport in semiconductors we consider the transport of charge by the movement of electrons in the conduction band and movement of holes in the valance band [15].

During the transport of the charge throughout the material, phonons are created. These phonons result in an increase of the temperature of the material, introducing thermal conduction [19]. At thermal equilibrium the carriers follow Boltzmann distribution which is a function of the temperature of the system. [20]. These hot carriers are responsible for the decrease in the efficiency of the photovoltaic cells. These hot carriers exist in the system for a few hundred picoseconds or longer before they can recombine. These hot carriers produce electric currents. If we could be able to capture all the energy from the hot carrier and transfer to electric energy the efficiency of the solar cell would rise about 66% rather than the present efficiency of just 31% [21].

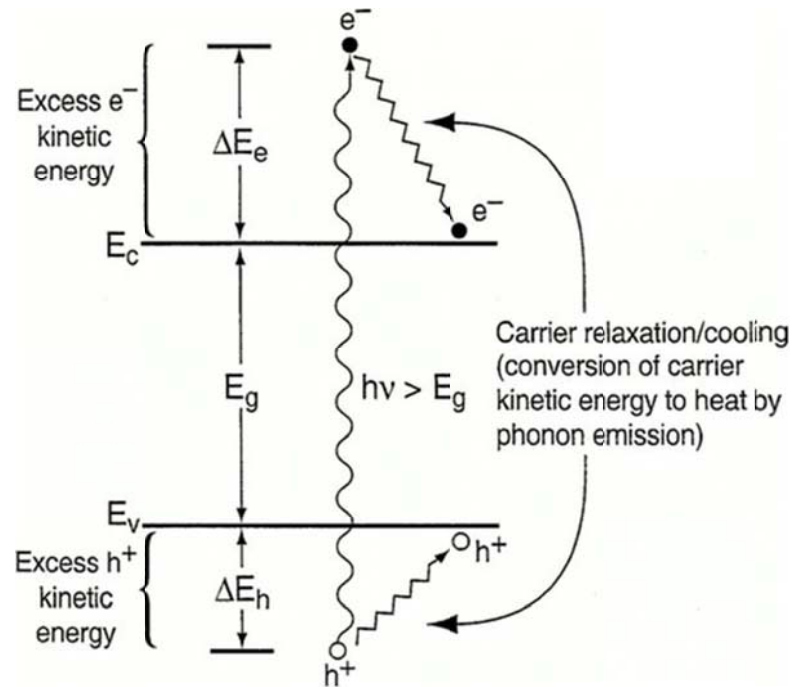


Figure 1.4: Hot carrier relaxation/cooling dynamics in semiconductors [22]

The transport described is the classical description of the carrier transport in a material. But for our purpose of study we need to understand the transport in the interfacial region. Various interfaces will be described in the following section. But let us understand the transport phenomena first. When the carrier transfers from an one material to the allowed state in the another material without any change in energy or without any tunneling it is called thermionic emission [15].

### 1.2.2 Application of Semiconductors:

Semiconductors can be widely used in electronics and optoelectronic devices. The applications of the semiconductors depend on the capability of the device to form various electrical junctions. These barriers or junctions are usually the principal source of

photovoltaic actions in solar cells [11]. The junctions important to us are described below.

***i) p-n junction***

A p-n junction in a semiconductor is formed by bringing different semiconductors with two opposite charges together. Simply, it is a close contact between p-type (positive charge) carriers and n-type (negative charge) carriers. In charge carriers diffuse across the junction. The electrons from the n-type material diffuse to occupy the space available in the p-type material, and the holes diffuse to the n-type material. This diffusion process leaves ionized shallow donor and acceptor levels, respectively [10-11, 23]. During the diffusion the electron and hole encounter each other and recombine, this forms a region around the junction called the *depletion region (W)*. The interface is now depleted of charge carriers. This establishes the *space charge region (SCR)*. The p-n junction is explained much clearer in the Figure 1.5. The concentration of the donor ( $N_d$ ) and the acceptor ( $N_a$ ) play an important role in the space charge region [23].

In Figure 1.5, we can visualize that when the two types (n-type and p-type) of semiconductors are brought together, the Fermi-level of both the semiconductors will equilibrate at the same level. Since this requires the Fermi level to be constant across the junction, *band bending* is necessary (Figure 1.5 (b)). The bending does not occur in the physical form in the system but in these diagrams we can see the bend of the curve.

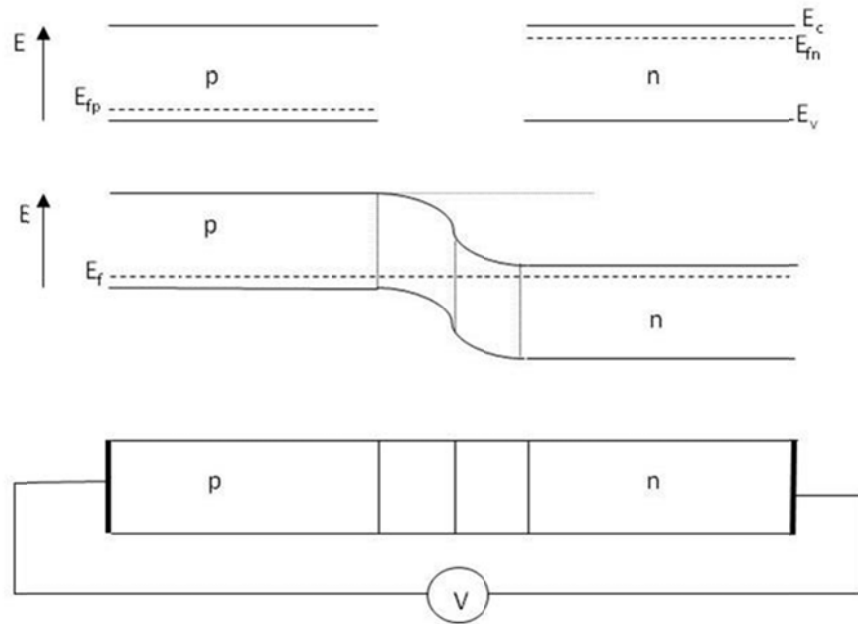


Figure 1.5: Schematic representation of *p-n junction*: (a) energy level for p-type and n-type semiconductors, (b) energy level for the same material after they are brought together to create junction (in thermal equilibrium), and (c) p-n junction showing space-charge carrier (or depletion region) [23]

Similar movement occurs in the semiconductor in the presence of phonons. The band bending of the material follows the same principle of the Fermi level change. The junction property under both illuminated and dark conditions needs to be studied for the photovoltaic application. An electronic symmetry in the semiconductor is required for the photovoltaic application.

## ii) Schottky Junction

The junction containing a metal and a semiconductor with a depletion region (Schottky barrier) is called as the Schottky junction, also referred as the metal-semiconductor diode structure [23]. In this type of junction a potential drop occurs in the

interfacial region due to the work function differences. Due to the difference in the availability of the charge carriers, the potential drop occurs on the semiconductor side of the junction as shown in the Figure 1.6(a). Here the metal acts as a highly doped semiconductor affecting the electrostatic properties of the depletion layer [24].

The less concentrated charge carrier (minority carriers) in the semiconductor acts like that of in p-n junction. For example, in absence of the source the minority carrier concentration at the edge of the depletion region depends exponentially on the applied voltage, with an exponential decay into the bulk. When it comes to the majority charge carrier transport, the only obstruction it faces is the depletion region potential barrier at the interface. The height of the barrier varies with the voltage applied to the system (Figure 1.6 (b and c)).

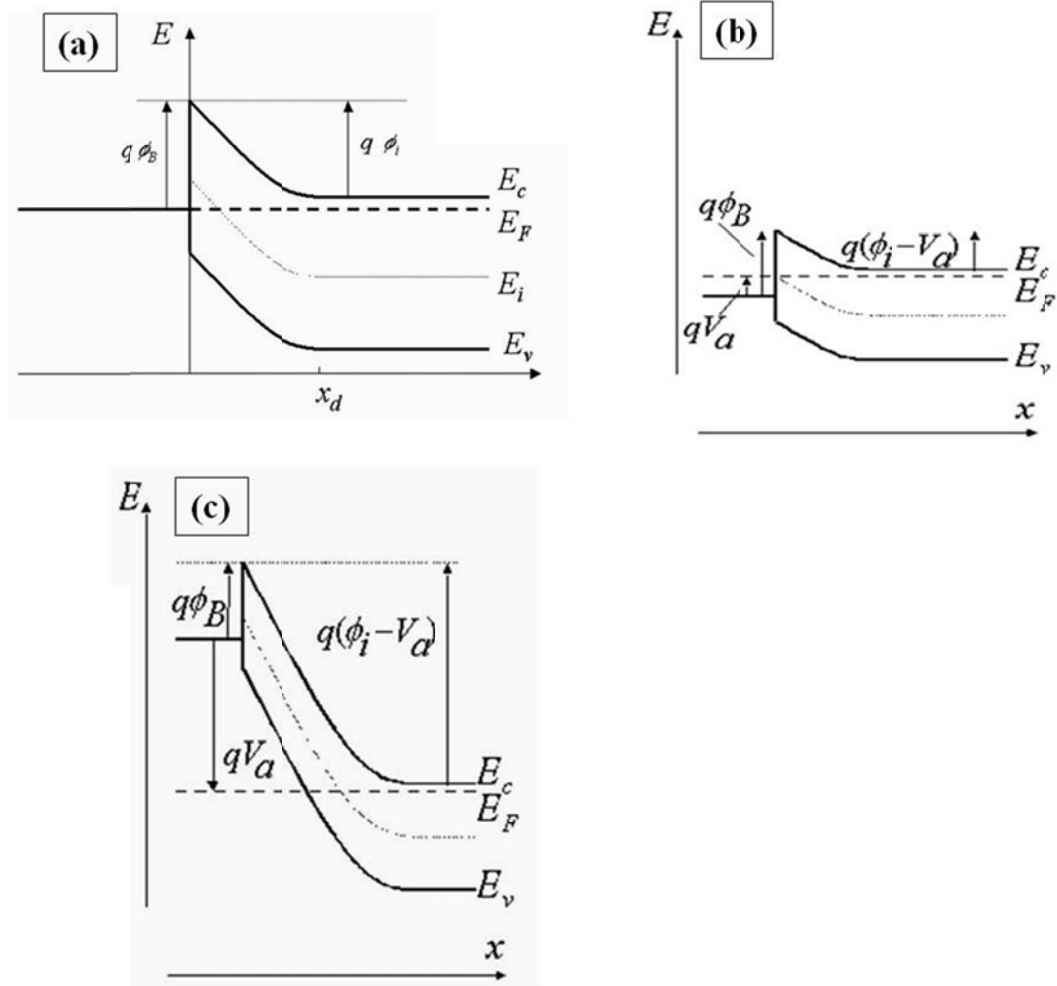


Figure 1.6: Energy Band diagram at a metal-semiconductor heterojunction: a) at thermal equilibrium, b) at forward bias and c) at reverse bias. Where:  $\Phi_b$  is the height of the barrier,  $q$  is the electron charge [25]

The current component of the majority carrier is larger than the minority carrier component as shown in Figure 1.7(a) below. This excess current carrier component is utilized to increase the dark saturation current of the diode which decreases the open circuit potential. Therefore it is undesirable for the photovoltaic energy conversion [24-25]. Studies show that the larger the barrier,  $\Phi_b$ , the better the performance of the system.

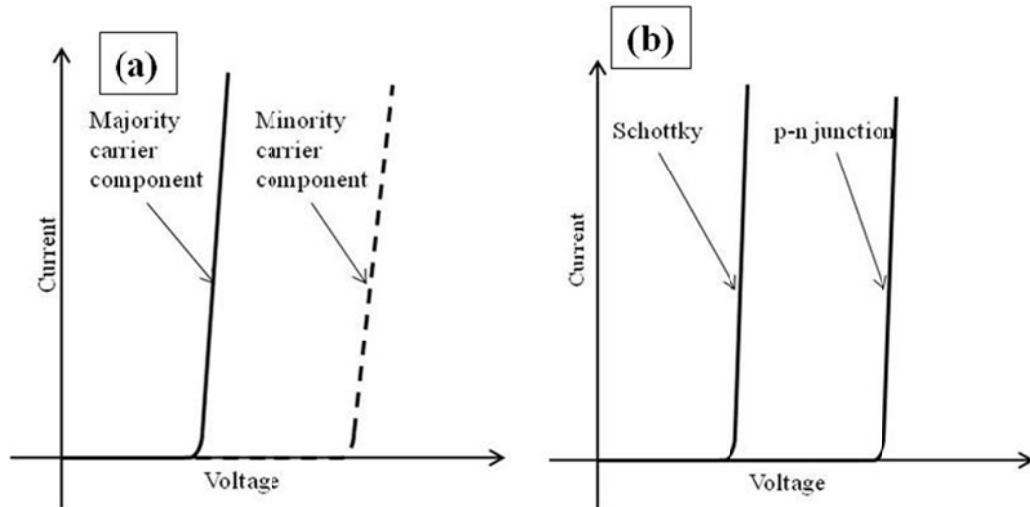


Figure 1.7: (a) Current component in Schottky diode in dark. (b) Comparison of the illuminated characteristics of Schottky and p-n junction devices [17]

### **iii) Metal-insulator-semiconductor (MIS)**

The metal semiconductor junctions (Figure 1.8) are not very suitable for the application in solar cells. The interfacial barrier is not strongly dependent on the work function of the metal as expected from the theory. Therefore an insertion of thin film insulating layer, the junction can be made very useful [11].

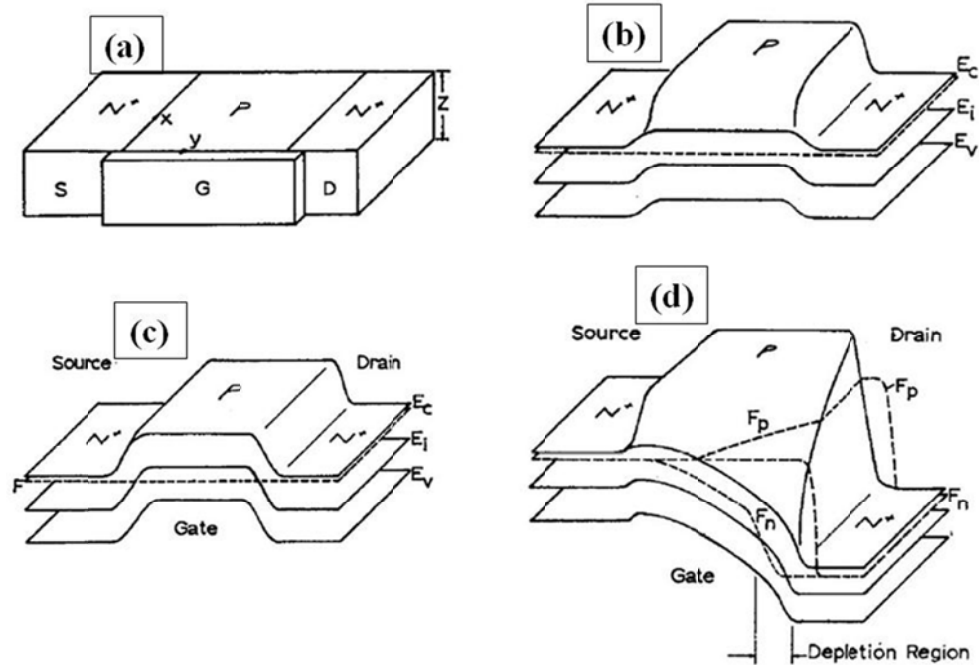


Figure 1.8: (a) Typical sketch for a MIS semiconductor. 3-D Energy band diagram at the (b) equilibrium condition, (c) equilibrium condition under a gate bias and (d) equilibrium condition under both drain and gate bias [26]

The insulating layer is typically very thin; therefore it allows the carriers to flow through the quantum mechanical tunneling as shown in the Figure 1.9. It is simple quantum mechanical phenomena where the carriers tunnel through the barrier. The carriers tunnel because the total mechanical energy of the carriers is lower than the potential energy of the barrier [27]. The decrease in the insulator thickness increases the current flow in the semiconductor [28-29].

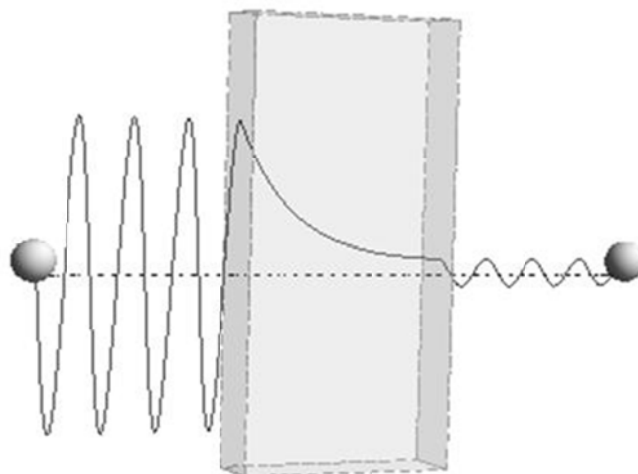


Figure 1.9: Schematic representation of quantum tunneling through a barrier [30]

### 1.2.3 Photoelectrochemical cells

#### *i) Semiconductor-liquid Heterojunction*

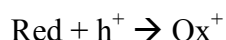
In the presence of a liquid electrolyte, a potential barrier is created on the surface of the semiconductor. The fabrication of these semiconductors requires somewhat less material processing. These semiconductor-liquid heterojunctions have been reported to have energy-conversion efficiencies in excess of 12% [17]. The major disadvantage of this approach is that the material is highly susceptible for photo enhanced corrosion. When combined with a conducting counter electrode, the system can be used to produce electricity or to generate hydrogen by photoelectrolytic decomposition of water [31].

#### *ii) Electrochemical Photovoltaic Cells*

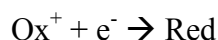
In this type of cell, the electrolyte consists of both oxidized and reduced state. The electrolyte in the cell acts as the charge transfer medium between the metal and the

semiconductor. If the species accept electrons then it goes to the reduced state; if it gives up an electron or accepts the hole then it oxidizes. These are referred as the *Redox couples*. The energy level of this redox couple ideally lies near the energy level of the minority carrier band edge of the semiconductor.

Under illumination the minority charge carriers generated in the semiconductor move to the solid-liquid interface, and are transferred across. For example for an n-type material, the holes from the semiconductor transfers through the interface oxidizing the reduced form of the couple.



Meanwhile at the counter electrode, the electrons move from the metal to the oxidized form of the electrolyte and reduce it [32].

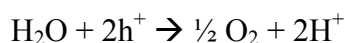


If a load is to be placed in between the two terminals of the metal and the semiconductor, the circuit will definitely be complete, and power will be supplied in a conventional solar cell.

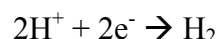
### **iii) Photoelectrolysis Cell**

The photoelectrolysis cell is similar to the electrochemical cell described above. This type of the cell can be used to produce chemical fuel, most commonly hydrogen by the photoelectrolysis of water. Here, the reactions take place in a similar manner as described in the previous section; for n-type material, oxidation occurs at the semiconductor

interface and the reduction occurs at the metal interface. But the reacting species are different. For example, for water splitting, the reaction taking place at the semiconductor is,



And at counter electrode,



The energy difference associated with these reactions is 1.23 eV. This states that the semiconductor with band gap larger than this energy is found to be corroded [17, 33].

These various types of systems (homogenous or heterogeneous) provide us with the possibility of fabricating photovoltaic cells of different kinds. Various laboratory studies have proven these technologies can be used in a cell with good efficiencies. As the technology advances better cells are generated.

### **1.3 Working Principles of Solar Cells**

Semiconductors absorb the photons from incident solar radiation only if they have energies larger than the band gap ( $E_g$ ) of that particular material. As shown in Figure 1.10, the photons with less energy slip through the material without being absorbed. Whereas the photons with energy greater than the materials' band gap creates an exciton. This absorption creates a negative electron on the conduction band and leaves positive hole on the valance band of the semiconductor [22, 34-35]. As this occurs, the excess

energy is distributed between the electron and the hole. This excess energy appears as the kinetic energy for the charge carriers (electrons and holes) [22].

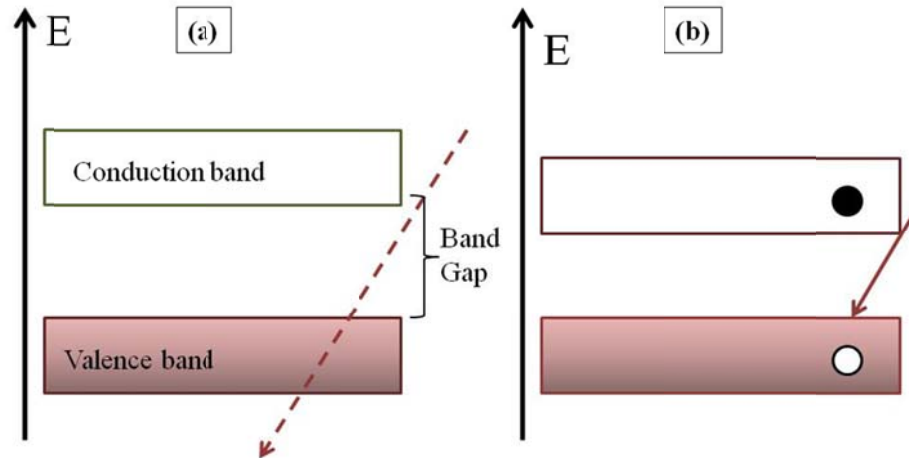


Figure 1.10: (a) Photon passes through—not enough energy to create an exciton (b) A photon with energy greater than the band gap energy—more than enough energy to create an exciton.

When light shines on a PV cell, electron-hole pairs across the entire device are generated. The creation of these multiple  $e^-h^+$  pairs in a bulk semiconductor has been studied for over 50 years [36]. The generated electrons move towards the n-type and the holes towards the p-type semiconductor [37]. If the device is open circuited, the electron hole pairs generated near the depletion region tend to recombine with the charge in the depletion region, thus reducing the depletion region charge and eventually reducing the depletion region. The reduction in depletion region is equivalent of applying a forward bias to the device i.e. this reduction in depletion region tends to develop a potential across the open terminals of the device. The maximum voltage that can be developed is the maximum forward drop across the device which theoretically is possible with the complete elimination of the depletion region. This maximum voltage that can be

developed across the open circuited device is called the open circuit voltage represented by the point  $V_{oc}$  in Figure 1.11. If the device is short circuited, the generated holes and electrons produce a current corresponding to the incoming photons. This current is called the short circuit current represented by the point  $J_{sc}$  in Figure 11. If any external load is to be placed then the ideal region of operation should be between  $V_{oc}$  and  $J_{sc}$ . The current flows through the device which creates a drop across the load and the direction of the current is such that the system comes into forward bias condition. As there is some drop across the load and the device, the maximum output voltage is not equal to the open circuit voltage. The forward bias conducts the device in the direction opposite to the current generated by the photons called the dark current. The presence of the dark current does not allow the device to operate at short circuit current. Thus the device operates in the fourth quadrant where the voltage is positive but the current is negative making the power negative, i.e. the device generates power from a light source [17, 38-39].

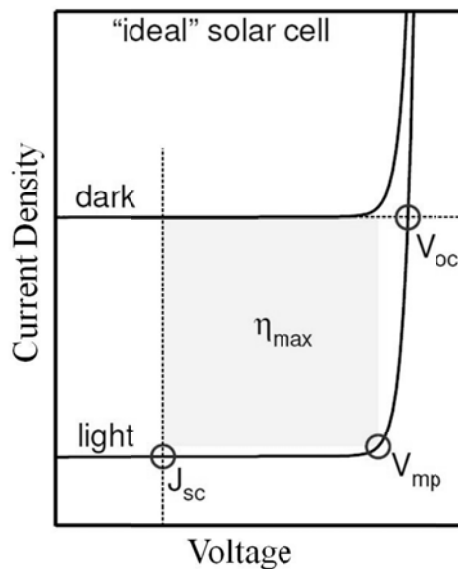


Figure 1.11: The Current vs Voltage plot for an ideal solar cell under both illuminated and dark conditions. In the graph,  $\eta$  is the efficiency of the solar cell.

### 1.4 Development in PV cells:

There have been various improvements in the renewable sources of energy like wind, sun etc. Solar energy has been getting the most attention among all other clean renewable sources because it is cheaper than the other alternative sources. The technology has been evolving in a very high rate. The classical cell started out with the silicon wafer based cell. The silicon cell still exists along with the thin film technology. For the production of high performance, low cost photovoltaic cells gave rise to the third generation photovoltaic. Photovoltaic (PV) research, development and industry have been expanding rapidly for a number of years now. Figure 1.12 shows how the bulk Si cell was slowly replaced by the nanostructured cell with time.

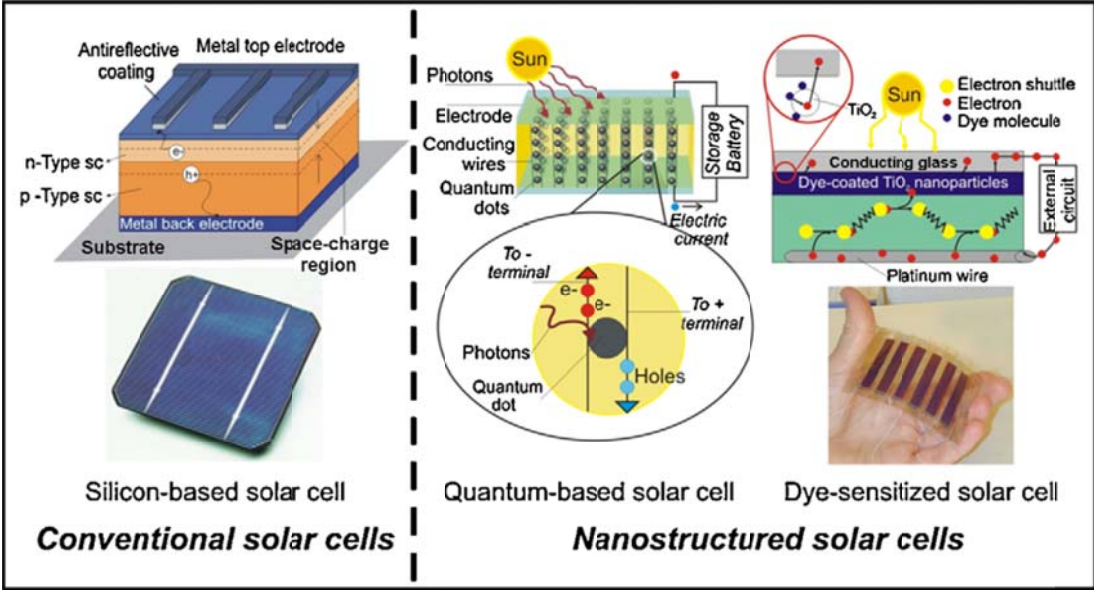


Figure 1.12: Evolution of PV technology: from Silicon based solar cell to nanostructured solar cells [9].

## **1.5 Types of solar cells**

### **First Generation: Silicon Solar Cells**

Crystalline silicon cells have been the most common type solar cells. Most solar cells sold in 2003 were Si-based solar cells, and they were classified as the first generation technology. These solar cells are manufactured using pure silicon. They use single junction for extracting energy from photons and are very efficient. These solar cells are comparatively large in size. This type still dominates in the commercial market despite their cost due to their high efficiency. The cost associated with the manufacturing of first generation solar cells is extremely high. The efficiency of the first generation solar cells is not expected to go more than 16% [7].

### **Second Generation: Solid State Thin Film PVs**

The second generation of solar cells has been under intense development from the 1990s through early 2000s. They are often referred to as the thin film solar cells. These types of solar cells are significantly cheaper compared to the first generation cells, because the designs use minimal materials and cheap manufacturing processes. The thin film of any semiconductor is always cheaper than that of the bulk counterpart. Another advantage of this over the previous type is its flexibility; thin film technology provides lightweight, aesthetically pleasing products. The most successful second generation materials are cadmium telluride (CdTe) that has proven its potential for high scale manufacturing [40] and copper indium gallium selenide (CIGS) that although currently holding a record efficiency for the second generation laboratory scale cells, has not seen a

major commercial success yet. Amorphous silicon and micromorphous silicon are also promising.

A standard example of second generation cells would be the solar cells made by Nanosolar Inc, which uses a special machine to print the cells at a fast rate. Though these cells have only 10-15% conversion efficiency, the decreased cost more than makes up for this deficit, and it is thought that second generation solar cells will surpass first generation cells in market share sometime around 2010. Second generation solar cells have the potential to be more cost effective than fossil fuel, though this may not occur until 2015 or later.

### **Third Generation: Quantum Dot PVs**

Third generation solar cells are still in the research phase, and so they are not available commercially. These are the cutting edge of the solar technology. These solar cells may not be just based on Silicon. The potential solar materials for the third generation solar cells are Dye Sensitized semiconductors, polymers, nanocrystalline materials etc. Technologies associated with third generation solar cells include multi-junction photovoltaic cells, sequence cells, nanostructured cells to better pick up incident light, and using excess thermal generation to enhance voltages or carrier collection [7, 41].

The goals of third generation solar cells are low-cost and high efficiency cells. The third generation solar cells approach is based on the hot electrons aspect. In these types of cells, the sun's energy is stored in the vigorous motion of the photoexcited

carriers. Some analysts predict that third generation cells could start to be commercialized by 2020. More about these types will be discussed later.

### 1.6 DSSC (Dye-Sensitized Solar Cells):

The DSSC is a relatively new class of low cost solar cell, which belongs to the group of thin film solar cells. In 1991, Gratzel et al first reported the dye-sensitized nanocrystalline  $\text{TiO}_2$  solar cells (DSSCs). These solar cells were based on the mechanism of a fast regenerative photoelectrochemical process [42]. The DSSC is different from the other classical solid-state solar cells with regards to both structure and working principles. The DSSC is an electrochemical solar cell. DSSC has two transparent conducting electrodes, a dye-covered nanocrystalline titanium dioxide ( $\text{TiO}_2$ ) layer and a liquid electrolyte is encapsulated (Figure 1.13).

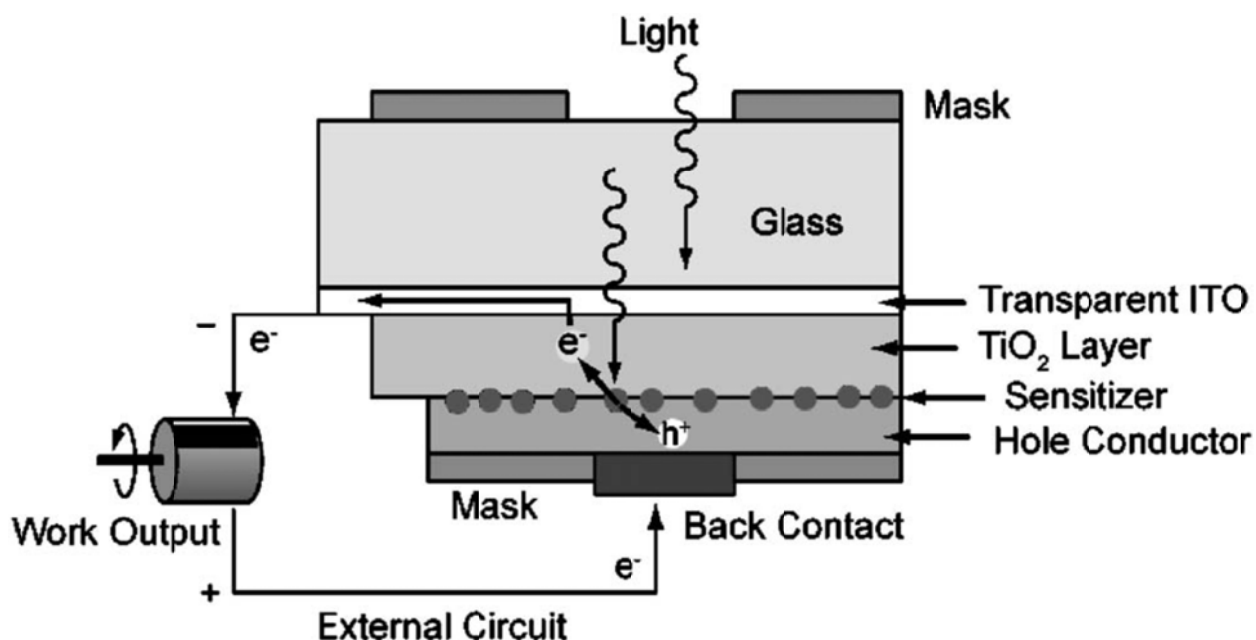


Figure 1.13: Structure of solid-state dye-sensitized nanocrystalline  $\text{TiO}_2$  solar cells [43]

The fundamentals of DSSC can be understood better with a sound knowledge of the basics of several technologies, such as nanoparticles, electrochemistry of redox electrolytes; catalysts and dye synthesis. The DCCS technology has captivated many scientists around the world. There have been a lot of investments and extensive research done in better understanding and optimizing the DSSC. Long term stability is a crucial requirement for solar cells and has shown improvement throughout the research [44]. Wang et al-Dokserv reported a stable 8 % efficient DSSC based on a low volatile electrolyte under thermal stress of 80 °C for 1000 hours [45]. It may be stated, that the fundamentals of the single cell are understood reasonably well and that a single DSSC is a controllable system.

Although the discovery of the DSSC was made almost two decades earlier, there is still a huge leap to be made between the laboratory research on single DSSC and the technological development of large area DSSC modules. A central issue of large area DSSC modules is that, although stable single cells have been demonstrated there lacks new module-related degradation mechanisms occurring in a series connection of DSSCs.

The research for finding the higher efficient solar cells has lead towards the study of nanostructured materials. For the past few decades the interest towards the semiconductor nanomaterials has attracted a wide range of researchers. The potential use of their electrical, magnetic, catalytic and optical properties in comparison with their bulk properties is the key motivation for the increase in research [46-47]. The materials tend to change their properties as they are sized down to nanometer scale [48]. Researchers are taking advantage of the change in properties of the materials after its decrease in size.

Specific applications of these structures are still the main focus for various companies [49]. Studies have proven that the semiconductor materials exhibit quantization effect in nanoscale when the electronic particles of the materials are confined by potential barriers to very small regions of space [34].

In the present work, we focused on the material for photovoltaic cell, and primarily on the nanostructured heterojunction. Researchers argue that the impact ionization in bulk semiconductor is not a meaningful approach to increase the efficiency of the PV cells [35]. Therefore the interest has moved on towards the nanocrystals of the semiconductors. The efficiency ( $\eta$ ) of a solar cell can be described as,  $\eta = (\text{Power}_{\text{out}}) / (\text{Power}_{\text{in}})$ . The limitation for efficiency of the ordinary solar cells is the band gap of the semi-conducting material. The efficiency of a PV cell can be increased by arranging a series of semiconductors (i.e. operating a cell with a series of different PV cells). In theory, the maximum efficiency that a solar cell fabricated with single semiconductor material can achieve is about 32% (Shockley's Theory). But in practice it is only about 25%. The efficiency can be definitely improved by stacking with different band gap materials together creating a multi-junction cell. This stacking can theoretically increase the efficiency to more than 70% [36].

### **1.7 Quantum Dot Solar Cell**

For a nanostructured PV cell the efficiency can be increased by decreasing the phonon emission phenomena [50]. As we know phonons are the result of vibrations of the electrons in the material which may lead to an increase in the temperature of the material [51]. In the PV cells the phonons may be responsible for the loss of kinetic

energy created by the solar photons [50]. When the solar photons hit the semiconductor surface, the electron excites possessing a very high kinetic energy. The electrons are then referred to as *hot electrons*. To increase the efficiency these hot electrons are need to be utilized before the loss of energy as heat through phonon emissions [52]. Therefore, we have adopted the quantum dot technology to utilize these hot electrons to generate Multiple Charge Carrier Generation to increase the efficiency of the solar cells.

Among the nanocrystalline structures quantum dots are very attractive candidates for synthesis of wide band gap semiconductor nanocrystals as light harvesting assemblies [18, 53]. The interest and development on this particular area has continuously developed over decades. Various reports have been submitted over the characterizations of quantum dots (QDs). Quantum dots are reported to have advantage of a high extinction coefficient ( $\sim 10^5 \text{ dm}^3 \text{ mol}^{-1} \text{ cm}^{-1}$ ). According to Nozik [35, 41, 50], the multiple excitation generation (MEG) in QDs is very efficient and has lower photon energy threshold than compared to that of the bulk semiconductors. During the MEG process, a single photon of light of sufficient energy is absorbed by the quantum dot and produces more than one bound electron-hole pair, or excitons (Figure 1.14). This effect can be used for the power conversion efficiency of solar cells.

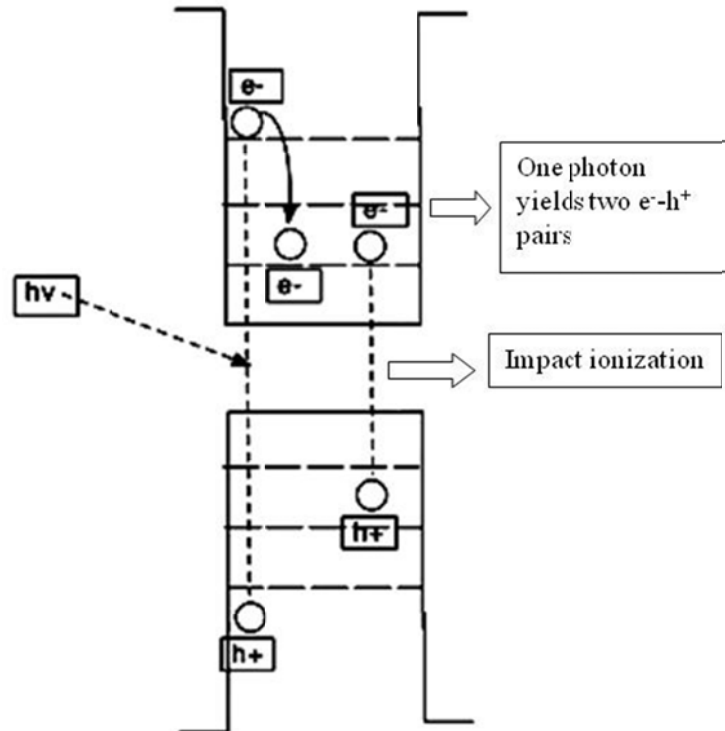


Figure 1.14: Photovoltaic efficiency enhancement for the quantum dot solar cell via impact ionization [54].

Quantum dots open up ways to utilize hot electrons and/or generate multiple charge carriers with a single photon [55-56]. The hot electrons (hot carriers) utilization for the higher efficiency of the solar cells can be done in various ways. Enhanced photovoltage and enhanced photocurrent are the two different approaches for this problem. For the enhanced photovoltaic, the extraction of the hot electron before they cool down is necessary [50, 57]. This can be also achieved by slowing down the cooling rate [52]. To achieve the enhanced photocurrent, the hot carriers are required to produce other electron-hole pair through impact ionization. For this to occur in a system, the rate of photogenerated carrier separation, transport and interfacial transfer across the

semiconductor all much be faster than the rate of cooling [22, 50]. As shown in Figure 1.14, the first electron-hole pair generated by the solar photon absorption is responsible for the other electron-hole pairs.

Quantum dots also possess a discrete quantized energy level, due to which the slow hot carrier cooling in the QDs can be utilized to enhance the efficiency of the quantum dot solar cell. The radiant energy can be converted to the electrical energy [34-35] utilizing QDs. The quantum dots material, exhibiting three-dimensional (3D) quantum confinement, are highly desired for their size-tunable optical properties. Synthetic routes utilizing organometallic precursors enable production of nanocrystalline particles with nearly monodisperse size dispersions [58-59]. The band gap of the QDs can be tuned by changing the particle size and/or by doping. The tuning of the quantum dots helps to optimize the performance. The purpose of the tuning is to tailor the QDs to absorb or emit specific wavelengths of light. The tuning can also be done by doping the QD material. The doped quantum dots capture the full spectrum sunlight and the nanotubes act as a tunnel for fast charge transport. Hence, quantum dots are offering the possibilities for improving the efficiency of flexible solar cells in at least two respects, 1) by extending the band gap of solar cells for harvesting more of the light in the solar spectrum, and 2) by generating more charges from a single photon. Reports also reveal that the physical and optical properties of QDs can be controlled by changing their size [60] .

In this work we discuss utilization of hybrid semiconductor materials (open nanotubes functionalized with low band-gap semiconductor quantum dots). The

quantum-sized particles (Q-particles) of PbS were embedded into porous TiO<sub>2</sub> films. Titanium dioxide (TiO<sub>2</sub>) and lead sulfide (PbS) have been reported to be important semiconductor materials, because of their superior optical, chemical and electronic properties [47]. The modified chemical bath process introduced by Plass [53] was used for the sensitization. For the uniformity of the particles on the nanotubes, ultrasonication was introduced. The lead sulfide (PbS) quantum dot deposition into a nanotubular structure of titanium dioxide (TiO<sub>2</sub>) will be presented herein.

Titania (TiO<sub>2</sub>) was chosen because of its high stability, favorable band gap energy, abundant availability and low cost [61]. Some of the other uses of TiO<sub>2</sub> include paints, body implants etc [62]. The crystalline TiO<sub>2</sub> nanotubes help in fast charge transfer, which increases the efficiency of the overall design. TiO<sub>2</sub> has a large band gap of 3.0-3.2 eV; therefore, it absorbs solar light only in the UV region [63]. The biggest problem is that only about 4-5% of the solar spectrum falls in this UV range. Various strategies have been applied by different researchers over the past few years to improve the photocatalytic efficiency, like changing the electrical properties of the TiO<sub>2</sub> by varying the crystallite size [64]. The classical approaches for the PV cells were based on the dye sensitization of nanocrystals or nanotubes [62]. Reports have been submitted that the successful QD sensitized semiconductor produce quantum yields greater than the one by impact ionization. Also the QDs give the tunability of the size by giving better optical range options and also a better heterojunction formation with solid hole conductors [22].

Among various nanoparticles, PbS has specific advantages. PbS possesses a narrow band gap of ~0.41 eV for bulk material and excitation Bohr radius of ~18nm [65].

The most valuable advantage of PbS for its quantum size is that it can effectively use the size quantization effect for extending the absorption into the infrared range that comprises of ~40% of solar spectrum [65-67]. The studies have also proven that the MEG effect in PbS Qdots opens the possibility of overcoming the ordinary thermodynamic limits of solar cells conversion [68]. Various scientists have faced challenges with quantum dots. The major challenge is the fast capture of electrons at the quantum dot interface. It has been studied that in mesoscopic films, the photogenerated electrons may have to encounter various grain boundaries and also many interfaces due to the random network of semiconductor nanoparticles. This increases the probability of the recombination with the photogenerated holes. This particular behavior may bring down the efficiency of the cell. This challenge can be improved by combining the QDs with another appropriate semiconductor [18], in our case TiO<sub>2</sub> nanotubes.

## Chapter 2: Materials and Methods

### 2.1 Materials and Chemicals Required

The base material or material substrate used was a Titanium (Ti) foil (99.99% purity) from EPSI-metals, Oregon, USA, with a thickness of 0.1mm. Reagent ACS grade ammonium fluoride ( $(\text{NH}_4\text{F})$  99.5%), ethylene glycol ( $(\text{C}_2\text{H}_6\text{O}_2)$  < 0.2 % water), cadmium chloride ( $\text{CdCl}_2$ ), lead acetate ( $\text{Pb}(\text{CH}_3\text{COO})_2 \cdot 3\text{H}_2\text{O}$ ) and lead nitrate ( $\text{Pb}(\text{NO}_3)_2$ ) were purchased from Fisher Scientific. Phosphoric acid ( $\text{H}_3\text{PO}_4$ ) 85% ACS reagents for the acidic anodization were purchased from Sigma-Aldrich. N, N-Dimethylformamide (DMF), thiourea and 1-thioglycerol for the reflux process of quantum dots deposition was purchased from Sigma-Aldrich too. Sodium sulfide ( $\text{Na}_2\text{S} \cdot 9\text{H}_2\text{O}$ ) and sodium thiosulfate ( $\text{Na}_2\text{S}_2\text{O}_3$ ) from Fisher Scientific were used for the photoelectrochemical characterizations.

### 2.2 Synthesis Procedure

#### 2.2.1 Preparation of $\text{TiO}_2$

Self ordered  $\text{TiO}_2$  nanotubes were obtained using an anodization technique. Titanium foils (Ti, 99.9%; EPSI-metals, Oregon, USA) were cut into squares the  $2 \times 2$  ( $\text{cm}^2$ ). These cut pieces were first polished using regular sand paper to get rid of any oxide layer, cleaned in acetone then processed for anodization. As shown in figure 2.1 the selected side to anodize is faced towards the cathode. The other side of the material is masked using the insulation tape.

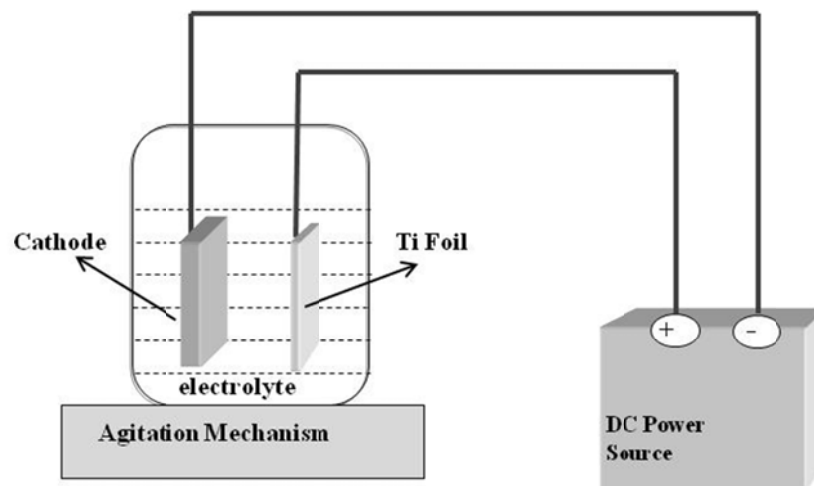


Figure 2.1: Schematic representation for the Anodization set-up for Ti foil

### 2.2.1.1 Synthesis of TiO<sub>2</sub> nanotubes in acidic anodization

The anodization was carried in an acidic solution under constant magnetic stirring. The Ti foil was immersed into the 0.5M H<sub>3</sub>PO<sub>4</sub> (phosphoric acid, Sigma-Aldrich, 85% ACS reagent) with 0.5 wt% NH<sub>4</sub>F (ammonium fluoride, Arcos Organics, 85%). The pH of the solution was read about 2. Another piece of Ti foil with greater area used to act as a cathode. The process was carried out for 45 min under constant supply of 20V with a rectifier (Agilent, E3641A). The anodization process was carried out at room temperature. The anodized samples were rinsed with DI water very carefully and were dried in an air oven.

### 2.2.1.2 Synthesis of TiO<sub>2</sub> nanotubes in organic fluoride solution

To understand the nanotubular structure better, the anodization electrolyte was varied. The second type of the anodization was carried out in the organic electrolyte containing 0.5 wt% NH<sub>4</sub>F and 3 vol percent water in ethylene glycol (organic electrolyte). Ti foils were cut into small pieces of about 2 cm<sup>2</sup>. The anodization

procedure in ethylene glycol ( $C_2H_6O_2$ , (Fisher certified), < 0.2 % water), ammonium fluoride ( $NH_4F$ , (Fischer certified), 99.5%), with water was carried out at the potential of 50V for 30 min. During anodization, instead of a magnetic stirrer (like in acidic solution), ultrasonic waves were irradiated onto the solution. The waves provide higher mobility to the ions inside the solution. The anodization current was monitored continuously keeping the voltage constant throughout the process. After an initial increase-decrease transient, the current reached a steady state value. The anodization was stopped after specific duration of reaching a steady state current value. The anodized samples were properly washed meticulously with distilled water to remove the excess obstructed ions and dried in air oven.

The anodized nanotubes tend to be amorphous in nature. Therefore a heat treatment was performed on the samples. The prepared nanotubes (NTs) were annealed in a computer programmed tube furnace. The heating and cooling ramp was set to  $1^\circ C/min$  to avoid any thermal cracking. Nitrogen ( $N_2$ ) atmosphere was set throughout the process after purging with UHP argon gas at 200 sccm for 30 sec. The constant temperature of  $500^\circ C$  was maintained for 3 hours to yield crystalline  $TiO_2NTs$ .

## **2.2.2 Introduction of Quantum Dots into the prepared $TiO_2$ nanotubes**

### **2.2.2.1 CdS sensitization in the nanotubes**

The prepared  $TiO_2$  films were then used to deposit the CdS quantum dots. A simple reflux process was used to deposit these Qdots into the nanotubes. The reflux process is a simple technique that can be carried out in any laboratory. In this process, the

solution is set to boil which evaporates and then a condenser is used to condense the steam back into the solution.

A triple neck round bottom flask (200mL) was used for this process. One opening of the flask was attached to the condenser where the cold water was flowing constantly as shown in Figure 2.2. The second opening of the flask was closed tight. The third opening was used to insert chemicals and nanotubes into the solution. 100mL DMF was used as the base solvent. The solvent was purged with  $N_2$  gas for about 20 minutes and was continued to flow throughout the experiment. 0.8g cadmium chloride ( $CdCl_2$ ) was then added to the solvent. After the solution turns homogenous, 0.47g thiourea was added to the solution. After completely dissolving the chemicals, the solution was heated until it refluxes (at this point the color of the solution becomes yellow). The annealed  $TiO_2$  nanotubes were then added to the solution. 0.48mL 1-thioglycerol was carefully added to the solution with the help of a syringe. The solution was allowed to stand for 5 minutes. The nanotubes composed with Qdots were then obtained. The surface of the samples seemed to get a yellowish green color (possibly due to quantum effect). The CdS-NTs were dehydrated in the desiccators.



Figure 2.2: The set-up for the reflux process: a triple neck round bottom flask connected with the condenser

The samples contain sulfur, which is not very stable. Therefore sintering is necessary to stabilize the sample. A tube furnace was used to sinter the samples in an Ar atmosphere at 200°C for 30 minutes, at a flow rate 200 sccm. The heating and cooling ramp was maintained at 3°C/min to avoid any thermal shock. Constant temperature and gas flow was maintained using the Nanolaunch computer program.

#### **2.2.2.2 PbS sensitization in the nanotubes**

From literature research and previous projects we have learnt that the  $\text{TiO}_2$  is a robust substrate. Nanoparticles can also be widely and uniformly distributed on the  $\text{TiO}_2$  surface. We started with CdS to have a better understanding of the surface mechanisms. Then we switched the material to lead sulfide salts. As we know that the lead salts possess strong quantum confinement due to the narrow band gap. The lower electron and hole mass of these salts make it a strong candidate to imply large confinement of energies, split equally between the carriers. For this project, PbS was deposited into the nitrogen annealed  $\text{TiO}_2$ NTs using two different techniques: reflux process and chemical bath deposition technique.

The reflux process used was similar to the CdS deposition. A triple neck round bottom flask (200mL) was used; attaching one opening to the condenser where the cold water was flowing constantly while the second opening of the flask was sealed tight throughout the experiment. The third opening was used to insert chemicals and nanotubes into the solution. 100mL DMF was used as the base solvent. The solvent was purged with N<sub>2</sub> gas for about 20 minutes. 1.67g Pb(CH<sub>3</sub>COO)<sub>2</sub>·3H<sub>2</sub>O was added to the solvent. Once the solution turned homogenous, 0.47g thiourea was added to the solution. The homogeneous solution was heated until it refluxed. The solution turned dark brown while heating. The annealed TiO<sub>2</sub> nanotubes were then added to the solution. 0.48mL 1-thioglycerol was carefully added to the solution with the help of a syringe. The solution was left to stand for 5 minutes. The nanotubes composed with PbS nanoparticles were then obtained. The PbS-NTs was dehydrated in the desiccators.

The size of the nanoparticles obtained after the reflux process were not under the quantum size level. Therefore a different technique of chemical bath deposition was used for sensitizing PbS into the TiO<sub>2</sub> nanotubes. For the chemical bath deposition a saturated lead nitrate solution was prepared. The solution was obtained by first dissolving 50g of Pb(NO<sub>3</sub>)<sub>2</sub> in 100mL of DI water. The solution was then heated and more Pb(NO<sub>3</sub>)<sub>2</sub> was added to the solution. The solution was then cooled to precipitate. The precipitate was then filtered off using Whatman filter paper. The TiO<sub>2</sub>NTs substrate electrodes were dipped for 1 min into a saturated lead-nitrate solution. The electrodes were then rinsed with water thoroughly. Then dipped into a 0.2 M Na<sub>2</sub>S solution and rinsed again with DI water. This is considered to be one cycle of deposition. It was noticed that different size

particles were obtained by repeating the coating procedure for different times. The final process was optimized with a total of 9 cycles. The UV-Vis and SEM characterizations were carried out for the optimization of the process.

The deposited particles tended to have agglomerated in some spots. To have the uniform distribution of the particles into the nanotubes the deposition environment was varied. The difference in the photoelectrochemical behavior was also studied under the variation of the environment of deposition. The deposition procedure was either carried out in an elevated temperature of 60°C and another set of material was prepared under the constant supply of ultrasonic waves for deagglomeration and uniformity of the particles.

## **Chapter 3: Characterization Techniques**

### **3.1 Scanning Electron Microscope (SEM)/Energy Dispersive Spectroscopy (EDS)**

The morphological study of the nanotubes and the synthesized quantum dots were carried out using cold field emission scanning electron microscope. A Hitachi S-4700 field emission scanning electron microscope was used for the analysis of composite morphology. An electron source gun fires a fine beam of electrons. The beam is controlled by the condenser lenses. The lenses demagnify the beam before it hits and scans the sample. The beam then interacts with the sample and sends out the signal off from the sample to the detector. At the same time, the spot of a cathode ray tube (CRT) is scanned across the screen while the brightness of the spot is modulated by the amplified current from the detector. The electron beam and the CRT spot are both scanned in a similar way to television receives in a rectangular set of straight lines known as a raster [69]. The image is then recorded.

Energy dispersive X-ray (EDX) analysis was done using an Oxford detector to study the composition of the material. EDX analysis provided the analytical scanning of the sample.

### **3.2 Transmission Electron Microscope (TEM)**

The prepared  $\text{TiO}_2$ -PbS was characterized under TEM to understand the crystal structure of the quantum dots sensitized nanotubes. The TEM was used only for the optimized PbS quantum dots.

TEM analyses of the samples with very high spatial resolution were performed. Information about the morphology, crystal structure and defects, crystal phases and

composition, and magnetic microstructure could be obtained by a combination of electron-optical imaging, electron diffraction, and small probe capabilities. TEM also provides significant in situ capabilities, allowing for the investigation of how material structure can evolve due to different environmental factors. The trade-off for this diverse range of structural information and high resolution is the challenge of producing very thin samples for electron transmission [69].

### **3.3 UV-Vis Measurement**

Diffuse reflectance ultraviolet and visible (DRUV-vis) spectroscopy was used to obtain the absorbance spectra for the prepared nanostructured semiconductor. The absorbance of light energy which excites the electrons from the ground state to the first singlet excited state of the material are measured. The DRUV-vis region of energy for the electromagnetic spectrum covers 1.5 - 6.2 eV which relates to a wavelength range of 200 - 800 nm. Diffuse reflectance UV-Vis spectra-photometry (Model: UV-2401 PC, Shimadzu Corporation, Japan) was used to carry out the studies on the samples. Powdered barium sulfate powder was used as a standard for the baseline correction in the scan range of 200-800 nm. The test confirmed that the material was active in the UV region.

### **3.4 Photoelectrochemical Measurements**

Experiments on photoelectrochemical were carried out in a glass cell using computer-controlled potentiostat (SI 1286, Schlumberger, Farnborough, England). The potentiostat controlled the potential and recorded the photocurrent generated in the cell. The cell comprised of a 60 mm diameter quartz window to shine the light on to the

sample. A 300 W solar simulator (69911, Newport-Oriel Instruments, Stratford, CT, USA) was used as a light source. The light at  $87 \text{ W/m}^2$  power level was passed through an AM 1.5 filter. The intensity of the light was measured by a thermopile sensor (70268, Newport) using a radiant power and energy meter (70260, Newport Corporation, Stratford, CT, USA). An interference filter (Edmund Optics, Kit # 55-223) was used to illuminate the surface of the electrode with light or specific wavelength intervals.

The cell comprised of 0.35(M)  $\text{Na}_2\text{S}_2\text{O}_3$  and 0.24(M)  $\text{Na}_2\text{S}$  electrolyte using a glass cell with Qdots sensitized  $\text{TiO}_2$  as anode and platinum foil as the cathode. A Ag/AgCl electrode was used as a reference electrode. Anodic voltage was applied to the samples under illumination at a scan rate of 5 mV/s while the photocurrent was recorded. A voltage of 0.2 V (Vs Ag/AgCl) was applied to the working electrode in the potentiostatic conditions to carry out the current transient experiments. The illumination time to the sample was controlled by manually switching the shutter of the solar simulator on and off at certain interval of time.

### 3.4.1 Corrosion Potential

Open Circuit Potential (OCP), measurements were carried out using a three-electrode system configuration, with Ag/AgCl in saturated polysulfide as a reference electrode, with and without illuminating the sample. Since both the  $\text{TiO}_2$  nanotubes and PbS QD loaded  $\text{TiO}_2$  show n-type conductivity, upon light illumination, the OCP values shifted to more negative values. The shift in the OCP [ $\Delta E = \text{OCP}(\text{with illumination}) - \text{OCP}(\text{without illumination})$ ] showed about the band bending of the samples at the electrolyte interface. Larger band bending resulted in generation of higher photo-

potential,  $\Delta E$ . The OCP was measured as a function of time by periodic interruption of the illumination. When the illumination was stopped, the OCP shifted to positive values and tended to reach its original dark-OCP value. The speed at which the illuminated OCP value reached the original dark-OCP value gave an idea about the electron-hole relaxation process in the material. The electron-hole relaxation upon interruption of light depends on the number of traps present in the material for recombination. Apparently this type of relaxation process will be slower than the electron-hole recombination occurring during the illumination condition

### **3.6 Impedance and Mott-Schottky Measurements**

Electrochemical impedance spectroscopy was carried out with and without illuminated conditions. The samples were maintained at OCP under illuminated and non-illuminated conditions. A 10mV AC signal was superimposed onto the OCP. Real and imaginary impedance values were measured by scanning the frequency of the AC signal from 10 KHZ to 0.01 HZ. The real impedance was plotted as a function of imaginary impedance. The real vs imaginary impedance plot is referred to as Nyquist plot. The plot gives an idea about the electrolyte resistance, to change transfer and impedance due to diffusion control.

Imaginary impedance values measured at a selected frequency as a function of applied potential can be used to calculate the capacitance of the space charge layer. From the capacitance values, Mott-Schottky plots are constructed. Here the capacitance of the double layer is ignored and  $1/C^2$  is considered to have a large contribution from the space charge layer.

The charge carrier concentration of the semiconductor photoelectrode can be calculated by the following equation by plotting the linear portion of the  $1/C^2$  Vs potential plot in both dark and illumination conditions.

$$N_D = \frac{2}{e\epsilon\epsilon_0 m}$$

Where,

$N_D$  = charge carrier density

$e$  = elementary electron charge

$\epsilon$  = dielectric constant and

$\epsilon_0$  = permittivity in vacuum

$m$  = slope of the  $1/C^2$  versus potential plot

Mott-Schottky analysis was carried out at a frequency of 3000 Hz while an AC signal of 10 mV amplitude was also overlaid on the applied DC potential. The DC signal was varied from 0.2 V to -1.5 V in steps of 50 mV with a time interval of 2 seconds.

### 3.7 Photovoltaic Study

Photovoltaic measurements were carried out on the prepared samples. The  $\text{TiO}_2$ -PbS active photoelectrode was characterized by front side illumination. A platinum electrode was used as the counter electrode for the system in a 0.35(M)  $\text{Na}_2\text{S}_2\text{O}_3$  and 0.24(M)  $\text{Na}_2\text{S}$  electrolyte. A two electrode configuration was used. In this method the prepared samples and the counter electrode is dipped into the electrolyte in a vessel. A

quartz window in the reactor cell allowed the light to strike the anode. The system was then connected to the computer-controlled potentiostat (SI 1286, Schlumberger, Farnborough, England). A 300 W solar simulator (69911, Newport-Oriel Instruments, Stratford, CT, USA) was used as the light source. The light at 87 W/m<sup>2</sup> power level was passed through an AM 1.5 filter. The intensity of the light was measured by a thermopile sensor (70268, Newport) using a radiant power and energy meter (70260, Newport Corporation, Stratford, CT, USA). The active area of the analyzed anode was 0.5 cm<sup>2</sup>.

## Chapter 4: Results and Discussion

### 4.1 TiO<sub>2</sub> Nanotubes

The nanotubular arrays were synthesized by electrochemical anodization using two types of electrolytes: 1) ethylene glycol containing 0.5 wt percent NH<sub>4</sub>F with 3 vol percent water at 50V for 30 min, and 2) 0.5M H<sub>3</sub>PO<sub>4</sub> with 0.14M NH<sub>4</sub>F at 20V for 40 min.

#### 4.1.1 TiO<sub>2</sub> nanotube array in Ethylene Glycol Solution

Vertically standing, self organized TiO<sub>2</sub> nanotubes arrays were obtained after anodization of the Ti metal. Figure 3.1 shows the SEM image of the top surface of the as-prepared self-assembled TiO<sub>2</sub> nanotubes. After the anodization process using ethylene glycol solution, the nanotubular array was annealed and then used to deposit the nanoparticles.

The ethylene glycol based preparation showed nanotubes having smoother outer wall surface than acidified fluoride based preparation method. Figure 4.1 shows the nanotubular morphology of ethylene glycol based method. The nanotubes had outer diameters ranging from 40-60 nm, tube wall thickness of 10-20 nm, and length of about 800 nm - 2 μm.

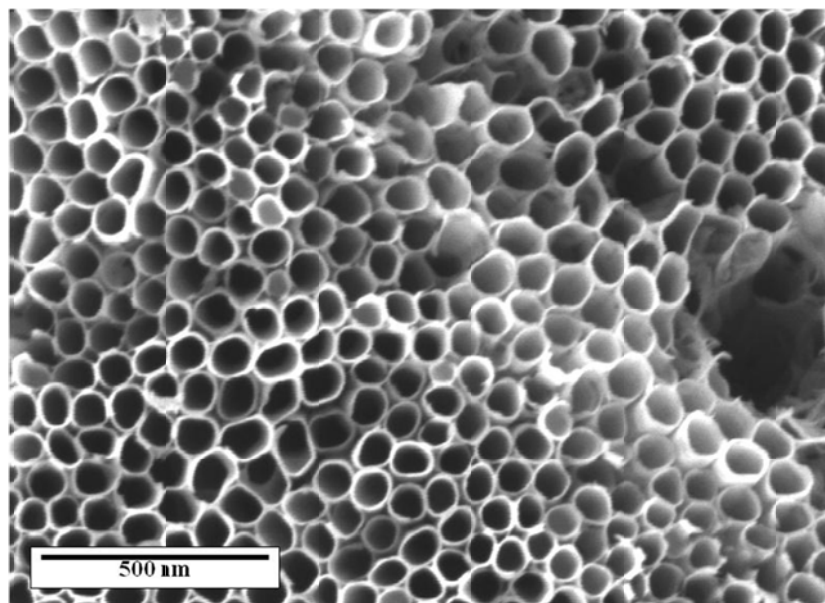


Figure 4.1: Top surface view of the nanotubular oxide layer on the Ti foil after anodizing in ethylene glycol solution. The diameter of the nanotubes were between the range of 60 - 80 nm

#### 4.1.2 TiO<sub>2</sub> nanotube array in Acidic Solution

Ordered nanotubular oxide layer at room temperature were prepared from an acid based electrolyte. The electrolyte was composed of 0.5M H<sub>3</sub>PO<sub>4</sub> with 0.14M NH<sub>4</sub>F and the anodization was run for 45 min at 20V. The main parameters controlling the reaction were electrolyte composition, anodization voltage, time and the agitation method. The composition of electrolyte allowed the ion incorporation onto the TiO<sub>2</sub> surface in subsequent growth of nanotubes. The nanotubes showed a uniform inside diameter of 60-70 nm.

The nanotubes prepared by acidified fluoride solution had larger diameter than those from the ethylene glycol solution, but had shorter length. The wall surface contained a number of ridges. The nanotubes prepared by acidified fluoride solution had diameters of 80 - 120 nm and lengths of about 400 nm (Figure 4.2).

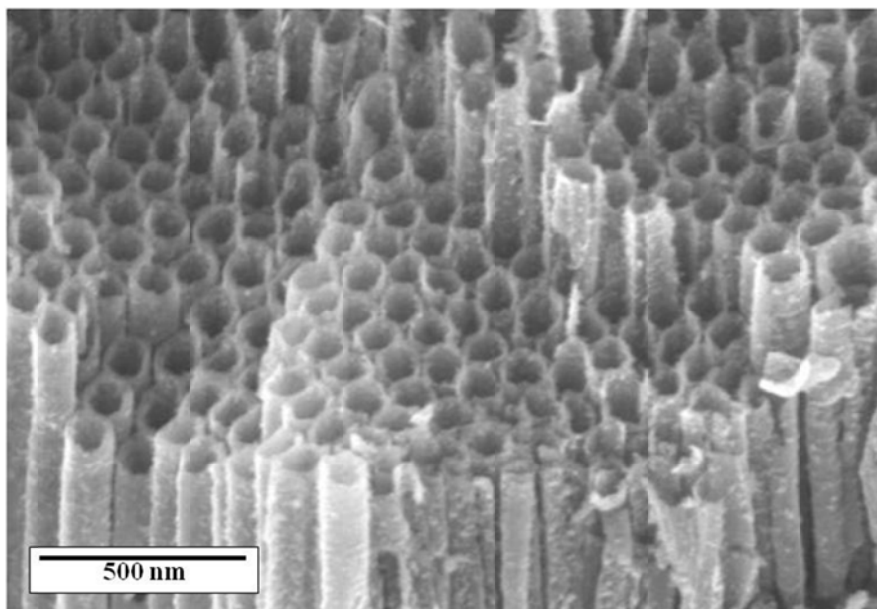


Figure 4.2: Top Surface morphology of the nanotubular oxide layer formed on the Ti foil after anodization in acidic solution. Self organized array of nanotubes with the diameter in the range of 70-90 nm. The nanotubes formed in acidic solution were a little wider than that formed in the organic solution (figure 4.1 above)

## 4.2 CdS introduced TiO<sub>2</sub> Nanotubes

Synthesis of the nanostructured compound using the reflux process with controlled morphology is well known [70-71]. In this project, we have prepared CdS NPs via the reflux process. Here we have tried to confine the architecture inside the nano channels of the prepared TiO<sub>2</sub> NTs array.

### 4.2.1 Morphological study conducted on CdS-TiO<sub>2</sub>

The morphological study of CdS deposited TiO<sub>2</sub> NTs was studied under SEM. Figure 4.3 shows the SEM images of the prepared CdS-TiO<sub>2</sub> samples. As time increases the CdS starts getting deposited on top of the already deposited CdS layer.

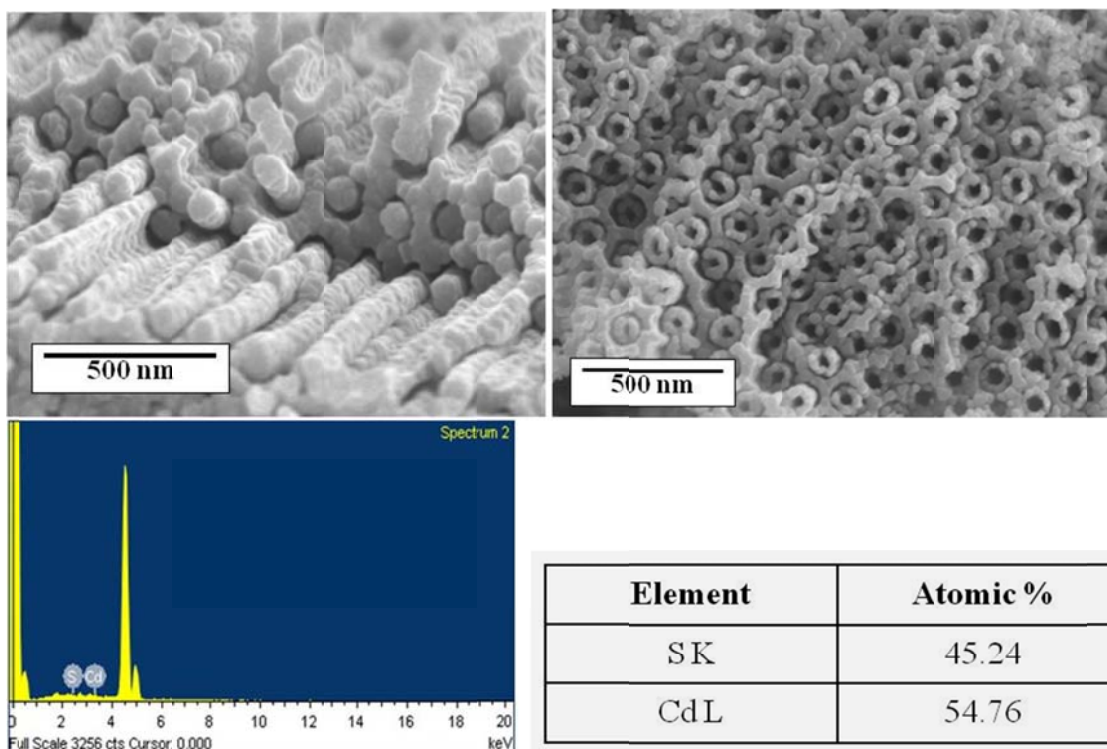


Figure 4.3: SEM image of as-prepared CdS-TiO<sub>2</sub> (a) side view for the composite prepared (b) top surface view for the CdS-TiO<sub>2</sub> as prepared. (c) Elemental analysis for CdS-TiO<sub>2</sub> confirming the presence of Cd and S at the ratio of almost 1:1. The SEM images show that the particles size are larger than intended but the elemental analysis prove that the materials still follow the required stoichiometric ratio

From the Figure 4.3(b) above we can conclude that the nanoparticles are deposited in a helical pattern. The CdS was deposited inside the nanotubes as a concentric tube. The particles get deposited into the nanotubes and are attracted towards the inside walls of the nanotubes. They follow the similar pattern throughout the process and acquire a helical path until the particles reach the top surface of the nanotubes.

#### 4.2.2 DRUV-VIS study for CdS-TiO<sub>2</sub>

The UV-Vis diffuse reflectance (or optical absorbance spectrometry) study was conducted on the samples to check its suitability for PEC or PV applications. Figure 4.5

shows the absorbance plot for the CdS-TiO<sub>2</sub> in comparison with pure TiO<sub>2</sub>. It is observed that the TiO<sub>2</sub> absorbs in the UV region with a band edge of 390 nm. Whereas, the test results of CdS-TiO<sub>2</sub> show that the composite material has a band edge of 547.5 nm. That is, the optical observance takes off at the band edge point.

From the Figure 4.4 we can observe that the on-set of absorbance occurred at about 547.5 nm for the CdS-TiO<sub>2</sub>. This results in a band gap of 2.26 eV. From the literature the band gap for CdS is 2.43 eV [61]. Therefore, Absorbance of light can be attributed to the light absorption of CdS.

$$\text{Band Gap} = \frac{1240 \text{ eV}}{\text{wavelength}} = \frac{1240}{547.5} = 2.26 \text{ eV}$$

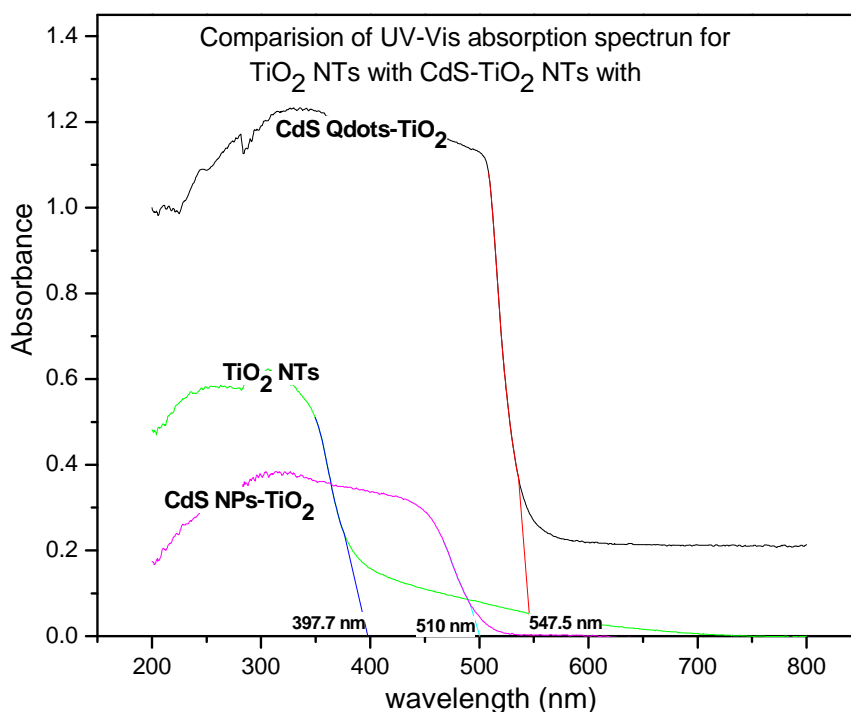


Figure 4.4: DRUV-vis spectra of annealed TiO<sub>2</sub> in comparison with CdS-TiO<sub>2</sub> NPs and CdS QDs

The Cds-TiO<sub>2</sub> absorbance spectrum showed a shoulder at about 390 nm which could be attributed to the absorbance by TiO<sub>2</sub>.

### **4.3 Studies performed on PbS sensitized TiO<sub>2</sub> nanotubes**

#### **4.3.1 SEM-EDX (PbS-TiO<sub>2</sub>)**

The morphological study of PbS deposited TiO<sub>2</sub> NTs was studied under SEM. Figure 4.5 shows the SEM images of the prepared PbS-TiO<sub>2</sub> samples.

The image (Figure 4.5) shows the morphology of the PbS deposited onto TiO<sub>2</sub> nanotubes by the reflux method described in the previous section. Briefly, in the reflux method, lead acetate dissolved in boiling DMF served as a source of lead. As the source of sulfur, thiourea and thioglycerol were added at a controlled rate to initiate the PbS nucleation onto the TiO<sub>2</sub> nanotubes. The PbS deposit obtained by the reflux method consisted of large particles of irregular shape. The deposit had two layered structure. The outer layer had uniform distribution of smaller particles. The size of the individual particles sitting on top of a thick inner PbS layer was in the range of 40-60 nm. The inner layer was neither continuous nor smooth. Some areas of TiO<sub>2</sub> nanotubes did not contain this type of coating morphology. Figure 4.5 (b) shows deposition of PbS crystals in patches. This bush type growth of PbS crystals occurred in top of the nanotubes in selected areas and the rest of the nanotubes were free of any type of PbS sensitization. The larger crystals PbS were in the size range of 100-150 nm with an aspect ratio of greater than 1.5. The particle size larger than 20 nm will not behave as a quantum dot and will not follow quantum mechanics [72].

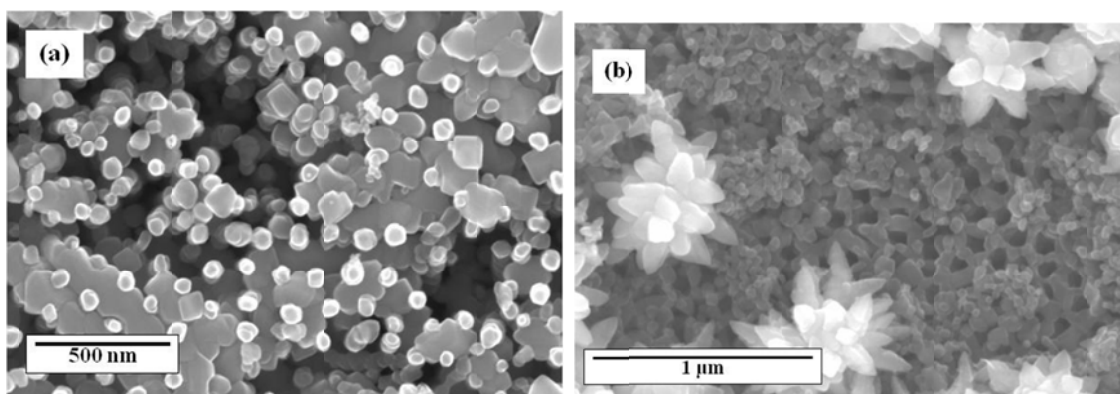


Figure 4.5: PbS nanoparticles formed after the reflux process.

Since the size of the PbS particles obtained by the reflux method was more than 50 nm, it was decided to vary the synthesis methods to produce nanoparticles of less than 20 nm diameter that would show quantization effect. The EDX result (Figure 4.6) shows that the bulk particles were still the intended PbS with the ratio of 1:1.

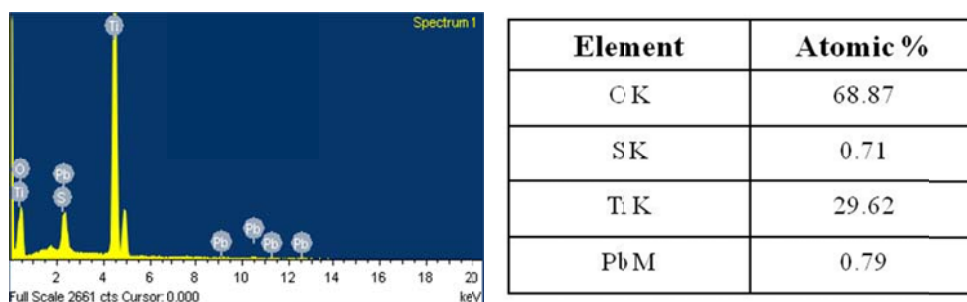


Figure 4.6: EDX analysis for the PbS-TiO<sub>2</sub> prepared via reflux process

The second PbS synthesis method investigated was a chemical bath method, called a successive ionic layer adsorption and reaction (SILAR), as reported by Lee's group [56].

The PbS particles obtained from this second process ranged from 5-15 nm depending on the number of cycles of SILAR deposition. It was observed that three cycles of SILAR coating did not result in the deposition of QDs. However, the coverage

of PbS on TiO<sub>2</sub> nanotubes was also very low at less than 15%, as seen in Figure 4.7(a). With the increase in the number of SILAR cycles, the size of particles and the coverage of the PbS onto TiO<sub>2</sub> increased. When the SILAR process continued for nine cycles under ultrasonication, the 100% coverage of the TiO<sub>2</sub> surface and large particles (>20 nm) were observed. Therefore, the number of cycles was limited to six.

Figure 4.7 (c) shows the image of the PbS nanoparticles precipitated on TiO<sub>2</sub> nanotubes by a SILAR method. The nanoparticles were observed to be distributed uniformly on the surface of the TiO<sub>2</sub> nanotubes. A surface coverage of 30-40% could be observed. Similar results were reported by H. Lee et. al [73]. The color of the samples also changed from the metal color to a dark brown color. The deposited particles seem to have given the color to the TiO<sub>2</sub> nanotubes. The color darkens with each cycle.

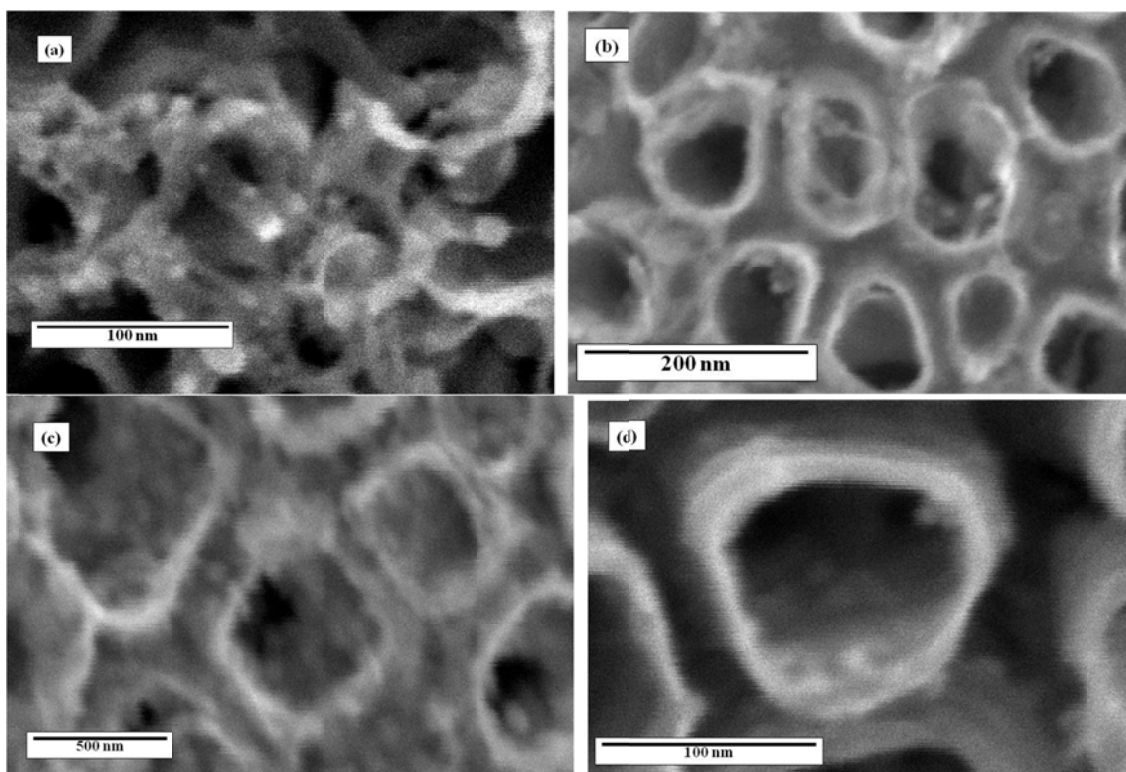


Figure 4.7: Morphology of PbS nanoparticles deposited in the TiO<sub>2</sub> nanotubes (a) QDs obtained after three SILAR cycles with less coverage, (b) The QDs being deposited inside the TiO<sub>2</sub> NTs, (c) PbS QDs onto TiO<sub>2</sub> NTs by a SILAR method where the uniformly distributed particles have a surface coverage of about 30-40%, and (d) PbS QDs of size less than 10 nm was obtained

Formation of chalcogenide compounds by SILAR process has been investigated by other researchers in detail. The mechanism of formation has been explained based on the ion-by-ion adsorption of the species onto the substrate. One complete cycle of SILAR process consists of the following essential steps [74].

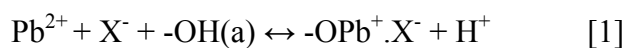
- 1) Immersion of the TiO<sub>2</sub> nanotubular substrate in a saturated solution of Pb<sup>2+</sup>
- 2) Monolayer adsorption of Pb cations on the TiO<sub>2</sub>
- 3) Removal of excess Pb<sup>2+</sup> by thorough washing with a solvent (this case ethanol)

- 4) Immersion of the monolayer  $\text{Pb}^{2+}$  cation adsorbed  $\text{TiO}_2$  nanotubular substrate in a dilute solution of  $\text{S}^{2-}$  anion
- 5) Preferential adsorption of  $\text{S}^{2-}$  anion at the  $\text{Pb}^{2+}$  sites
- 6) Reaction of  $\text{S}^{2-}$  with  $\text{Pb}^{2+}$  to form  $\text{PbS}$  compound
- 7) Thorough washing with the solvent (ethanol/water) to remove excess/unreacted sulfur anion

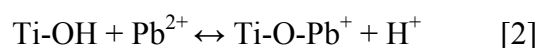
The above process steps suggested that the size of the  $\text{PbS}$  and the surface morphology could be controlled by tailoring experimental parameters such as concentration of cation, anion, immersion time and washing time. In addition, adsorption of  $\text{Pb}^{2+}$  on the  $\text{TiO}_2$  was an essential step that determines the uniformity in distribution of the  $\text{PbS}$  particles, size and stoichiometry of the  $\text{PbS}$  particles.

Adsorption of  $\text{Pb}^{2+}$  on to various oxides such as  $\text{MnO}_2$ ,  $\text{Fe}_2\text{O}_3$ , zeolite,  $\text{SiO}_2$ , and  $\text{Al}_2\text{O}_3$  has been investigated in detail mainly for water purification application. The important parameters that determine adsorption of  $\text{Pb}^{2+}$  onto oxides are pH of the solution, concentration, complexation, and contact time. However, pH independent adsorption behavior has also been observed at a particular pH range between 3.3-10.3 for magnetite ( $\text{Fe}_3\text{O}_4$ ) [75].

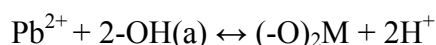
Two types of exchange reactions have been proposed for adsorption of  $\text{Pb}^{2+}$  onto the oxides. The first exchange reaction denoted as 1:1 is given as:



This reaction considers hydroxylation of the TiO<sub>2</sub> surface by chemisorptions of dissociated water molecules. Then the hydroxyl group adsorbs Pb<sup>2+</sup> by exchanging the proton (H<sup>+</sup>). This can be represented by the following Reaction [2] which is similar to the Reaction [1]



The 1:2 exchange reaction is given as :



It can be observed the 1:2 surface complex is neutral and the 1:1 complex has a positive charge which will be neutralized by a negative charge [76].

The formation of surface complexes of 1:1 or 1:2 can be visualized by considering the presence of Helmholtz electric double layers. When the TiO<sub>2</sub> nanotubes were immersed in lead nitrate solution, a Helmholtz double layer formed having Pb<sup>2+</sup> in the inner Helmholtz plane (IHP) and nitrate anions at the outer. The Pb<sup>2+</sup> cations were adsorbed on the TiO<sub>2</sub> because of electron transfer from the oxygen '2p' orbitals to the 'sp' orbitals of the Pb<sup>2+</sup>. The adsorption could occur preferentially at two sites: 1) Ti<sup>4+</sup> cation vacancy sites and 2) sites terminated with oxygen anion sublattice. In addition, geometrical defect sites such as pores, terraces, and ledges also could be preferential adsorption sites for Pb<sup>2+</sup>. Since Pb<sup>2+</sup> requires the least amount of binding energy to other divalent cations, adsorption of Pb<sup>2+</sup> occurs readily.

After the adsorption of the Pb<sup>2+</sup> on to TiO<sub>2</sub> nanotubes, the excess Pb<sup>2+</sup> cations were washed off. During this process, the nitrate anions could have been possibly washed out from the outer Helmholtz layer. Charge neutrality could be maintained by the

hydroxyl ions from the water used for washing. The ions in the outer Helmholtz layer could be replaced by the anions from the  $\text{Na}_2\text{S}$  solution such as  $\text{HS}^-$ ,  $\text{S}^{2-}$  etc, when the  $\text{Pb}^{2+}$  adsorbed  $\text{TiO}_2$  nanotubes were immersed in the  $\text{Na}_2\text{S}$  solution. Since the free energy of  $\text{PbS}$  formation is around  $-100$  kJ/mol at room temperature, bringing lead ions and sulfur ions together readily and rapidly forms a stoichiometric compound of  $\text{PbS}$ .

### **Effect of Ultrasonication**

Repeating the SILAR cycles a number of times resulted in an increased size of  $\text{PbS}$  particles and increase in surface coverage. No investigation was carried out to understand if the process followed Langmuir type adsorption isotherm. In order to have monodispersion particle size, the number of nucleation sites should be independent of immersion time and the number of SILAR cycles. The increase in the surface coverage should be attributed only to the increase the size of the  $\text{PbS}$  particles. However, in this investigation, a wider distribution of particles size was observed. This pointed out that new nuclei were formed with increase in the SILAR cycles under ultrasonic conditions.

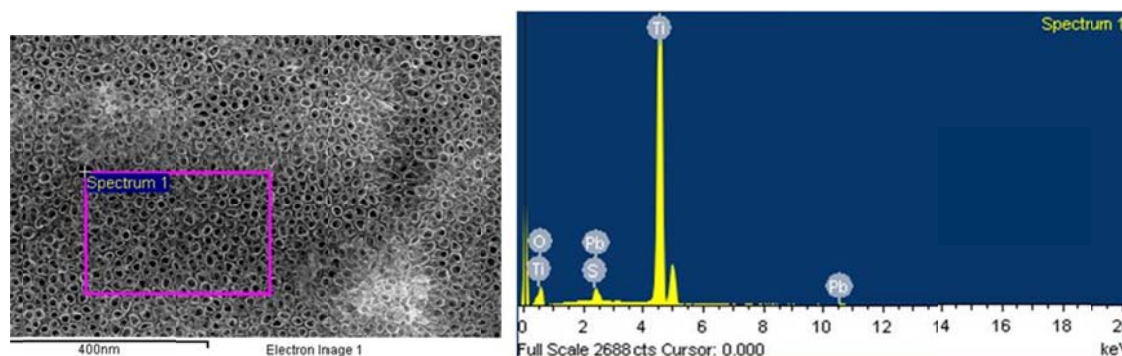
During ultrasonication new defect sites could have been created that acted as additional sites for  $\text{Pb}^{2+}$  adsorption. These sites were considered as cation vacancies because of dissolution of  $\text{Ti}^{4+}$  during ultrasonication. In addition, creation of new oxygen lattice sites on the  $\text{TiO}_2$  nanotubular surface could occur by ultrasonication. This is attributed to the formation  $\dot{\text{H}}$  and  $\text{O}\dot{\text{H}}$  radicals in the water by ultrasonication waves. The hydroxyl radicals formed during the ultrasonic treatment helped creation of new oxygen sites in the  $\text{TiO}_2$  nanotubes. Creation of new sites for adsorption of  $\text{Pb}^{2+}$  as the

ultrasonication continued resulted in an increase in the number density of PbS particles and a wide size distribution of particles.

So far discussion has focused on the  $\text{Pb}^{2+}$  adsorption sites and how ultrasonication affected these sites. The sites for  $\text{S}^{2-}$  adsorption also need to be taken into account while considering the formation of new PbS nuclei during multiple SILAR cycles. It was possible that  $\text{S}^{2-}$  ions were adsorbed at the sites where  $\text{Pb}^{2+}$  ions were not present. If  $\text{S}^{2-}$  was adsorbed on the  $\text{Pb}^{2+}$ , the compound formation occurred.

If  $\text{S}^{2-}$  ions were adsorbed on the surface sites where oxygen vacancy or  $\text{Ti}^{4+}$  metal cations were terminated PbS compound formation could take place during subsequent immersion in the  $\text{Pb}^{2+}$  solution. However, formation of discrete nanoparticles PbS was observed on the surface of the  $\text{TiO}_2$  nanotubes, as against formation of a continuous film of PbS. This observation indicated that not all the adsorbed  $\text{Pb}^{2+}$  cations and  $\text{S}^{2-}$  anions were continuously participated in the formation of the final PbS nanoparticles. Only energetically favorable adsorbed ions grew into PbS nanoparticles. The exact mechanism of growth is not clear at this time. A systematic study is required which was not the scope of this thesis. However, it could be argued that electrostatic repulsion of ions of similar charge played a significant role in the formation of discrete particles instead of a continuous thin film. Furthermore, a competition between two adsorption mechanisms, such as 1)  $\text{Pb}^{2+}$  adsorption at the cation exchange sites and 2) surface complexation reaction involving hydroxyl ions, could have also promoted the formation of nanoparticles.

Figure 4.8 below shows the elemental composition (EDX analysis) of the of  $\text{TiO}_2$  nanotubes deposited with PbS nanoparticles after 6 cycles of SILAR process. The PbS particles showed exact stoichiometry.



Element	Atomic %
O K	54.68
S K	0.49
Ti K	44.34
Pb M	0.49

Figure 4.8: EDX analysis shows the presence of Pb and S for the PbS- $\text{TiO}_2$  NTs as prepared via chemical bath deposition

The  $\text{TiO}_2$ -PbS composite structure was annealed in an inert atmosphere to convert the PbS into a complete crystalline structure. The thermal annealing was carried out in a tubular furnace with a controlled atmosphere of argon gas at a rate of 200 sccm. The samples were heated to  $350^\circ\text{C}$  at a rate of  $3^\circ\text{C}$  per minute, soaked at this temperature for 1h and cooled to room temperature at the same rate as the ramping. The resulted PbS nanoparticles showed a crystal structure of face centered cubic.

### 4.3.2 TEM (PbS-TiO<sub>2</sub>)

The annealed TiO<sub>2</sub>-PbS was characterized under TEM to understand the structure of the quantum dots. Figure 4.9 (a) and (b) show the HRTEM images of the PbS nanoparticles deposited onto the TiO<sub>2</sub> nanotubes.

A uniform distribution of PbS nanoparticles could be observed on both inside and outside surfaces of the nanotubes. The particles showed a size range of 5-15 nm. Figure 4.9 (b) shows the HRTEM image of the lattice of the PbS particles. The interplanar spacings of the lattice fringes were calculated to be 0.34 nm and 0.31 nm corresponding to the (111) and (200) planes of the fcc structure of PbS. The TiO<sub>2</sub> nanotubes showed predominantly the anatase structure with lattice fringe spacing 0.38 nm associated with (101) plane of the tetragonal structure. The HRTEM images confirm that PbS particles were uniformly embedded in the TiO<sub>2</sub> nanotubes. Both the TiO<sub>2</sub> and PbS were crystalline. Further the lattice spacing of anatase (0.38 and 0.30) and PbS (0.34 and 0.30) matched closely so that embedding of PbS nanoparticles induced low strain at the interface and therefore it was coherent with the substrate. This coherent interfacial lattice structure would help charge transport with minimal recombination losses. The HRTEM image also indicated the interface of the PbS-TiO<sub>2</sub> was less distributed and good lattice spacing match was registered.

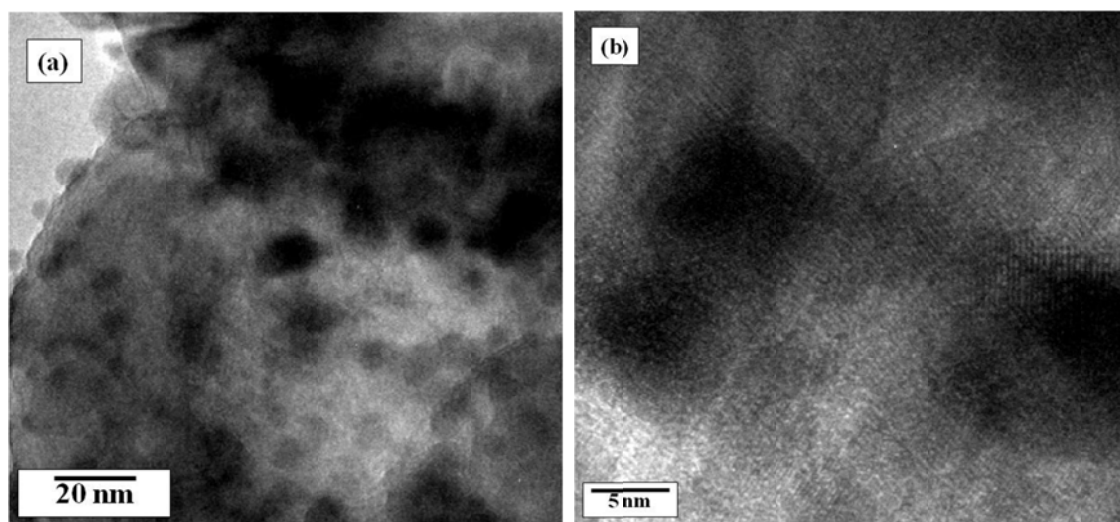


Figure 4.9 (a) and (b): HRTEM images for PbS deposited onto TiO<sub>2</sub> nanotubes

#### 4.3.3 Absorption study result for DRUV-VIS (PbS-TiO<sub>2</sub>)

The UV-Vis absorption study was carried out on the prepared samples. The PbS sensitization prepared via reflux process gave us a large band gap. Figure 4.10 shows the diffuse reflectance photo spectrometry of the TiO<sub>2</sub>-PbS sample prepared by the reflux (or colloidal deposition) method. TiO<sub>2</sub> nanotubes showed an absorbance take-off at about 390 nm. This corresponds to the band gap of anatase phase at 3.17 eV. Whereas, the PbS loaded TiO<sub>2</sub> showed absorbance at wavelengths longer than 800 nm. Since the UV-Vis photospectrometer used in this investigation was not capable of measuring absorbance of light in the infrared region ( $\lambda > 800$  nm), the exact absorbance take-off wavelength was not known. It should be noted that the band gap of bulk PbS was 0.41 eV that corresponds to a wavelength of 3024 nm. The absorbance at 800 nm indicates that the band gap of the TiO<sub>2</sub>-PbS system was smaller than 1.55 eV.

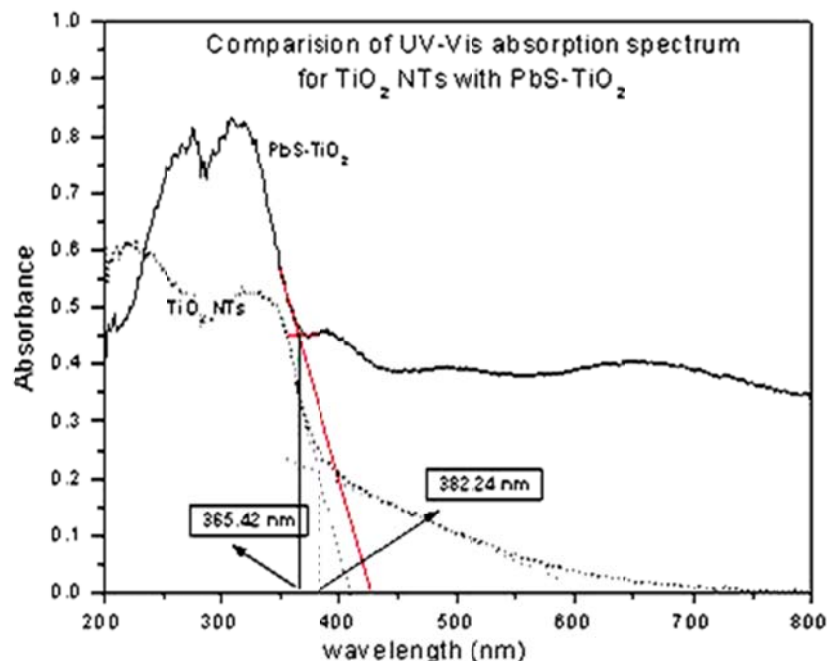


Figure 4.10: DRUV-vis spectra of the annealed  $\text{TiO}_2$  and  $\text{PbS-TiO}_2$  composite

Figure 4.11 shows the DRUV-Vis spectroscopic results of  $\text{TiO}_2$ - $\text{PbS}$  samples prepared by the SILAR deposition procedure. The absorbance of sample 1 with 3 cycles of SILAR in the as-deposited condition was not clear and indiscernible. The sample after 6 cycles of SILAR  $\text{PbS}$  deposition showed an absorbance spectrum with several shoulders at different wavelengths within 400-800 nm wavelength range. Below the 400 nm wavelength the absorbance was attributed to the  $\text{TiO}_2$  nanotubes. The origins of the shoulders of the absorbance spectrum at 650, 550 and 450 nm were not determined at this time. Surface analysis of the samples using XPS might produce some useful information about these shoulders, as these could be due to possible surface states such as adsorbed hydroxyl or oxygen. Possible oxidation of  $\text{PbS}$  surface could also result in such shoulders. Tang e.al. [77] reported the presence of  $\text{PbSO}_3$ , and  $\text{PbSO}_4$  in the  $\text{PbS}$  that introduced trap states. However, these  $\text{PbS}$  related defects could be observed only at

larger wavelengths (in the range of 0.8-1.3 eV, corresponding to 953-1550 nm).

Therefore, the shoulders observed at the shorter wavelengths could be due to adsorbed Pb and/or S ions that were not washed out during the SILAR process. These adsorbed species could have introduced surface states within the bandgap of TiO<sub>2</sub>. It should be noted that the onset of absorbance of these samples started at wavelengths longer than 800 nm in the as-deposited conditions.

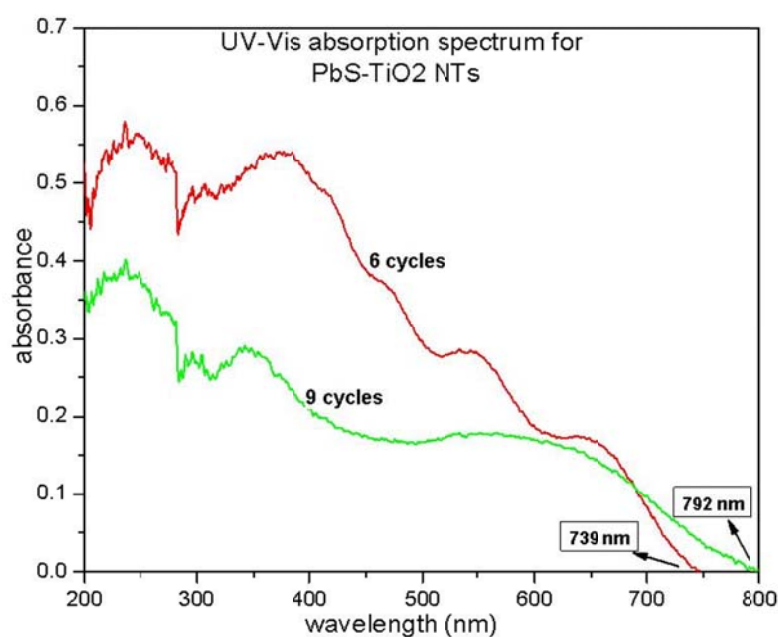


Figure 4.11: DRUV-vis of the TiO<sub>2</sub>, PbS-TiO<sub>2</sub> NPs, 6 cycles of chemical deposition and 9 cycles of chemical deposition resulted in various particle size range which showed in the difference in the on-set absorbance

Figure 4.12 shows the DRUV-Vis spectrometry results of TiO<sub>2</sub>-PbS samples after six cycles of SILAR and annealing at 200°C. For comparison, the results of as-deposited (not annealed) TiO<sub>2</sub>-PbS samples and TiO<sub>2</sub> nanotubes without any PbS are included. Both the samples (without and with annealing) showed almost similar spectrum of photo absorbance. The TiO<sub>2</sub> nanotubes were prepared by anodization in aqueous acidified

fluoride solution. The  $\text{TiO}_2$ -PbS samples without annealing showed about 25 nm red shift as compared to the annealed sample. Interestingly both the samples showed on-set of optical absorbance at wavelengths shorter than 800 nm indicating a significant quantum confinement effect.

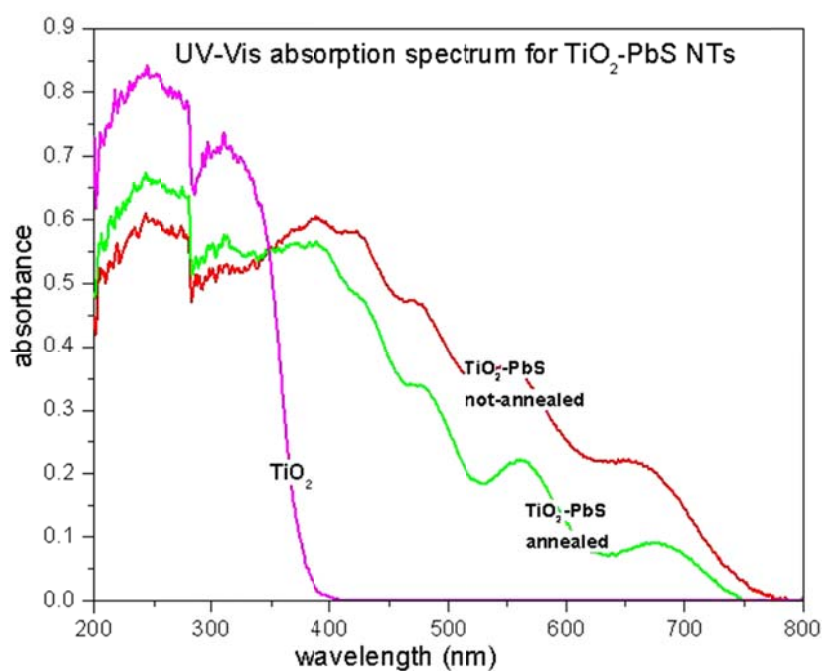


Figure 4.12: DRUV-vis spectra of the  $\text{TiO}_2$ ,  $\text{TiO}_2$ - PbS in comparison with the  $\text{TiO}_2$ -PbS annealed vs. the as prepared samples

Table 4.1 shows the band-gap calculations of different sensitized  $\text{TiO}_2$  samples, based on the on-set of absorbance wavelengths. It is evident that the  $\text{TiO}_2$ -PbS samples prepared by the SILAR method showed a strong quantum confinement as compared with other samples.

Table 4.1: Band gap comparison of DRUV-Vis data of TiO<sub>2</sub> NTs, CdSNP-TiO<sub>2</sub>NT and CdSQD-TiO<sub>2</sub>NT with the PbSQD-TiO<sub>2</sub>NTs annealed and as prepared samples

<b>Material</b>	<b>Absorption (nm)</b>	<b>Band Gap (eV)</b>
TiO <sub>2</sub> NTs	397	3.12
CdSNP-TiO <sub>2</sub> NTs	510	2.43
CdSQD-TiO <sub>2</sub> NTs	547.5	2.26
PbSQD-TiO <sub>2</sub> NTs (not-annealed)	790	1.57
PbSQD-TiO <sub>2</sub> NTs (annealed)	750	1.65

#### 4.3.4 PEC studies (PbS-TiO<sub>2</sub>)

##### *Corrosion Potential:*

The potential where the Fermi level of the electrolyte matches the Fermi level of the material is the flatband potential. The flatband potential is very important to understanding the Open Circuit Potential (OCP) of a material in an electrolyte. The corrosion potential study gives us the OCP for the dark and illuminated conditions. The change in Fermi Level at the equilibrium state provides OCP of the system. During our corrosion potential test we are also measuring the extent of band bending.

When in the dark (without illumination) the Fermi level of the material moves towards that of the electrolyte as the electrons jump to the conduction band and reaches maximum at the flatband potential. In the absence of the photon source the OCP of the n-type photoanode is less negative. As the sample surface is illuminated, the equilibrium potential moves towards more negative. The extent of the photoactivity of the electrode is understood by the difference between the two potentials. The better photoactivity of the material is considered for a larger negative shift.

During the process of the continuation and discontinuation of the photon source the disturbance in potential occurs providing the information about the charge generation, dynamics of recombination, existence of recombination centers, traps etc. When the light source is shined on the photoanode the electron hole pairs are created. And when that source is turned off the movement of the charge moves towards the positive charge as the electrons and holes created during photo-excitation recombine. As the experiment is continued the combination is complete and a plateau is reached in the OCP plot.

Figure 4.13 (a) shows the open circuit potential transient of the TiO<sub>2</sub> nanotubular sample prepared in 0.5 M H<sub>3</sub>PO<sub>4</sub> + 0.5 wt% NH<sub>4</sub>F solution and annealed in N<sub>2</sub> atmosphere at 500°C for 3h. The PEC measurements were carried out in a 0.35 M Na<sub>2</sub>S<sub>2</sub>O<sub>3</sub> + 0.24 M Na<sub>2</sub>S solution. The photopotential ( $\Delta E$ ) developed at the TiO<sub>2</sub>-polysulfide electrolyte interface with AM 1.56 simulated solar light illumination was -0.52 V. The transient potential profile upon illumination showed an abrupt negative shift in the potential indicating accumulation of the electrons at the electrode surface and shift in the Fermi level. Followed by an abrupt shift of -0.44 V that occurred in less than a second, further shift of -70 mV occurred relatively slowly for about 10 seconds. This slow shift in the potential could be ascribed as slow filling of electron traps that resulted in slow rise of the Fermi level.

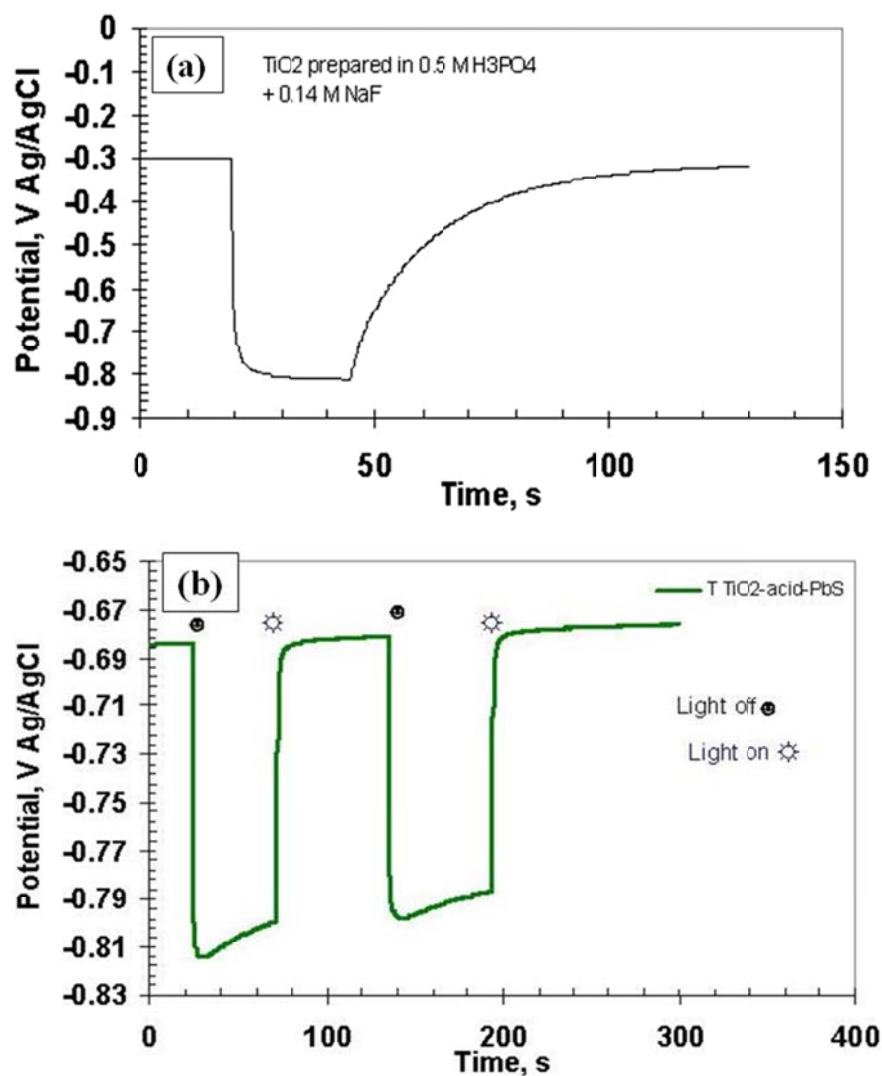


Figure 4.13: Open Circuit Potential plots with and without illumination (a)  $\text{TiO}_2$  nanotubes prepared by anodization of Ti in  $\text{H}_3\text{PO}_4$  with M NaF solution; (b) PbS- $\text{TiO}_2$  composite as prepared.

When the light illumination was interrupted the open circuit potential shifted in the positive (anodic) direction. The original OCP value that was observed before illumination (here after referred to as ‘Dark OCP’) was reached slowly. It took more than 60 seconds to reach back the dark OCP. The slow reversal of OCP upon interruption of the light indicates the slow equilibration of Fermi level of the semiconductor with the

electrolyte. The slow equilibration could be attributed to the surface states present in the TiO<sub>2</sub> nanotubes that hindered the Fermi level equilibrium process by momentarily pinning the Fermi level. Furthermore, it also indicated longer minority carrier life time in the material. When the light was interrupted the excess electron-hole pairs, generated by the previous light illumination process, were removed by a recombination process. This recombination occurred at the recombination centers or the site present in the TiO<sub>2</sub> material. In a semiconductor, the recombination depends on the probability of the majority carriers finding minority carriers at their trap sites. If the density minority carrier trap sites are high, the recombination will occur fast. On the other hand, if the density of the majority carrier trap sites (electron traps) are high, the recombination will occur slower because electrons should be released from the traps before they recombine. Therefore, the slow reversed of OCP upon light interruption could be attributed to the possible low density of hole traps or high density of electron traps. Metal cation vacancies can act as hole traps and oxygen vacancies act as electron traps. Anodized TiO<sub>2</sub> nanotubes contained a large concentration of oxygen vacancies.

Figure 4.13 (b) shows the potential transient profile of the TiO<sub>2</sub>-PbS sample. Since the size of the PbS nanoparticles was in the range 5-15 nm, less than the Bohr radius of the PbS material (22nm), quantization effects were anticipated. Therefore, the PbS prepared by the SILAR process, here after will be referred to as PbS QDs. It is interesting to note that the potential transient showed abrupt breaks upon light illumination and interruption. The generated photopotential ( $\Delta E$ ) was smaller than that observed with TiO<sub>2</sub> nanotubes without PbS sensitization. The smaller value of photo

potential indicated reduced band bending upon sensitization of TiO<sub>2</sub> with PbS. Since the band gap of PbS is much smaller than TiO<sub>2</sub>, the magnitude of band bending also is small. The quick recovery of the OCP to the original dark OCP upon the removal of light illumination indicated that the recombination of e-h pairs occurred very fast because of a large concentration of recombination centers present in the PbS QDs.

It should be noted that in PbS QDs, electron-hole pairs were present in the bound state as excitons. When light illumination was interrupted, the recombination process occurred at a faster rate because of the ability of the excitons to recombine easily. The samples showed an on-set of absorbance at around 800 nm. Since QDs are considered to generate multiple excitons per photon when the energy of a photon exceeds  $2E_g$ , where  $E_g$  is the electronic band gap of the semiconductor [78]. Therefore, the UV region of light could result in generation of at least 2 excitons per photons having  $E_{hv} > 3.2$  eV. Alternatively, the excess kinetic energy of the electron hole pairs generated by the photons ( $> 3.3$  eV) could be tapped as hot electrons with increased photogenerated potential. However, the  $\Delta E$  value observed was only about 150-200 mV, as shown in Figure 4.14 (for annealed samples), which indicates that the hot carriers were not extracted.

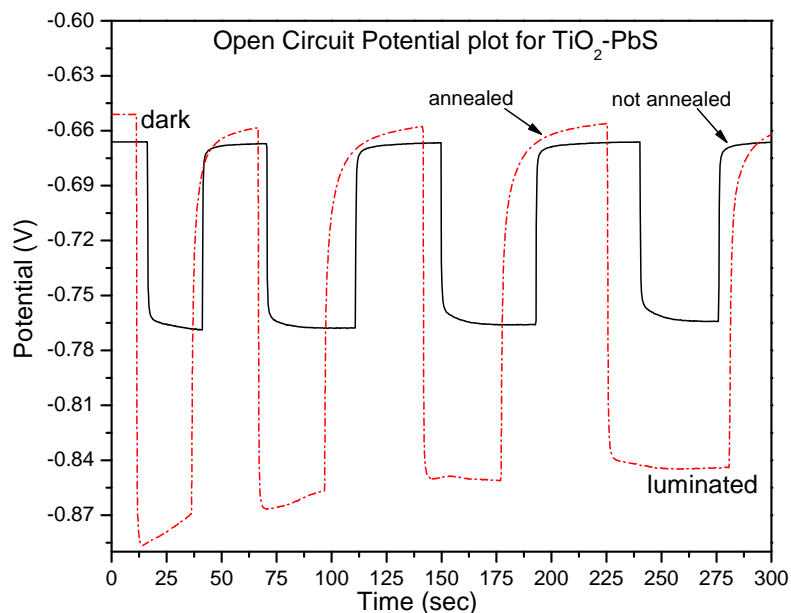


Figure 4.14: Comparison between the annealed and non annealed PbS-TiO<sub>2</sub> samples to study the Open Circuit Potential plots with and without illumination. The annealed samples were annealed in inert Argon atmosphere at 200 °C for 2 h.

Analysis of the potential vs current results will show whether multiple excitons are generated in the TiO<sub>2</sub>-PbS composite electrode material or not.

#### *Potentiodynamic:*

A potentiodynamic study is used to study the photocurrent generation behavior of the material as a function of applied potential. Figure 4.15(a) shows the potential vs current plot of TiO<sub>2</sub> nanotubes prepared in acidified fluoride solution and annealed in nitrogen. Illumination of light on the TiO<sub>2</sub> nanotubes generated electron-hole pairs. The holes were consumed in a possible oxidation of S<sub>2</sub>O<sub>3</sub><sup>2-</sup> into SO<sub>3</sub><sup>2-</sup> as well as oxidation of S<sup>2-</sup> into SO<sub>3</sub><sup>2-</sup>. In the process H<sup>+</sup> ions were generated. The electrons were separated by an internal electric field generated across the TiO<sub>2</sub> nanotubes and flew through the external circuit and reached the Pt electrode (cathode). On the cathode, the electrons participate in

the reduction of  $\text{S}_2\text{O}_3^{2-} + \text{H}^+$  ions back to  $\text{S}^{2-}$  and water. The flow of electrons in the external circuit was recorded as current in the plot illustrated in Figure 4.15 (a). When the illumination was switched off the electron flow diminished to a great extent as seen in the figure. Increase in the anodic potential increased the current values in spite of a constant illumination flux. The increase in the current could be attributed to the increase in the internal electric field in the  $\text{TiO}_2$  nanotubes that effectively separated the electrons from holes.

Figure 4.15(b) shows the potential-current plot of  $\text{TiO}_2$ -PbS sample using a three electrode test configuration. The  $\text{TiO}_2$  nanotubes were prepared in acidified fluoride solution and PbS was coated on to the  $\text{TiO}_2$  from a nine cycle SILAR process. The PbS QDs were annealed at  $200^\circ\text{C}$  for 2 hours in an inert atmosphere. Increase in the potential in the positive direction (anodic polarization) increases the current. The total current density observed with the  $\text{TiO}_2$ -PbS QD composite electrode was at least 6-8 times higher than that observed with unsensitized  $\text{TiO}_2$  (i.e. without PbS sensitization) nanotubes. The total current has two components: 1) photocurrent and 2) background current (or dark current) due to an external bias potential. In case of the unsensitized  $\text{TiO}_2$  nanotubes the dark current density was significantly less than that of  $\text{TiO}_2$ PbS QD composite electrode increased with increase in anodic potential. This could be attributed to the oxidation of PbS. Nevertheless, the photocurrent also increased with increase in the potential indicating that internal electric field present in the PbS QD played a significant role in the charge separation. The photocurrent density (determined by subtracting the dark current from the total current) at 0.2 V (Ag/AgCl) was about  $2.4 \text{ mA/cm}^2$ . This

value was almost an order of magnitude higher than that of  $\text{TiO}_2$  nanotubes under similar test conditions. This increase in the photocurrent value could be attributed to the higher light harvesting capability of the PbS QDs present on the  $\text{TiO}_2$  nanotubes. Furthermore, Multiple Exciton Generation (MEG) within the PbS QDs cannot be ruled out. Recently Sambur et al [78] reported absorbed photon-to-current efficiency (APCE) of about 200% for PbS QD decorated anatase (001) electrode. Similar effect could be possible with the  $\text{TiO}_2$  nanotubular PbS QD composite electrode also.

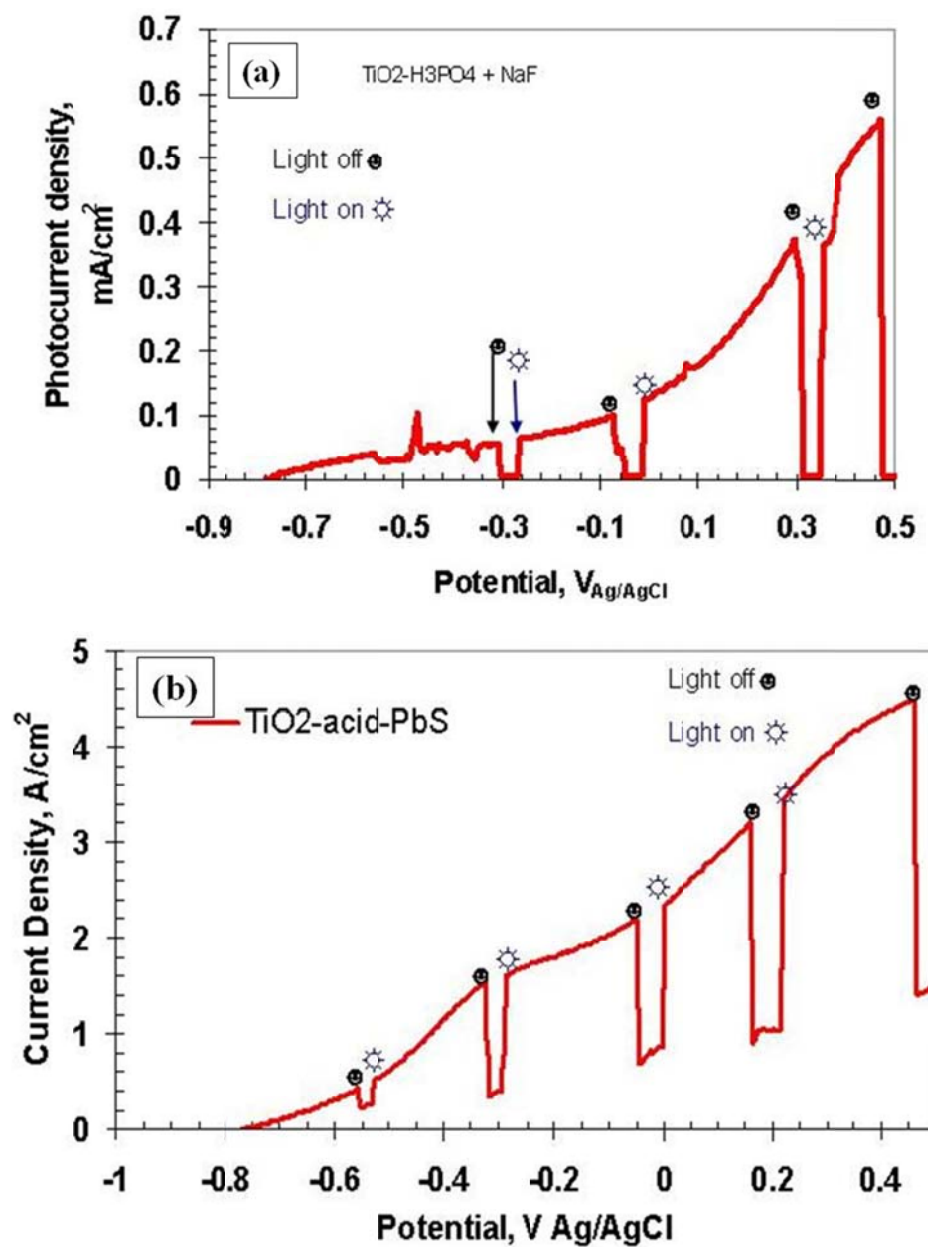


Figure 4.15: Photocurrent generation characteristic of PbS-TiO<sub>2</sub> NTs as a function of applied potential in the polysulfide electrolyte under AM 1.5 light illumination. (a) TiO<sub>2</sub> nanotubes prepared by anodization of Ti in H<sub>3</sub>PO<sub>4</sub> with NaF solution; and (b) PbS-TiO<sub>2</sub> composite as prepared. The nanotubes were annealed in inert Argon atmosphere at 200 °C for 2 h

*Potentiostatic:*

The potentiostatic study was used to study the stability behavior of the materials prepared. The potentiostatic (current vs time) plot (Figure 4.16) shows the photocurrent generated with and without the illumination on the photoanode. The Figure 4.17(a) shows the current transient plot obtained at a constant potential of -0.2V (Ag/AgCl), with and without light illumination of TiO<sub>2</sub> nanotubes that were prepared in acidified fluoride solution. A significant decrease in the current density was observed with time. Momentary interruption of light illumination resulted in the increase of current density which again decayed with time. After several on-off cycles, the current reached a quasi steady state condition. The reason for such decay is not known. However, saturation of surface anion vacancies with adsorption of S<sup>2-</sup> on the TiO<sub>2</sub> nanotubes could not be ruled out that resulted in the current decay. The reaction  $S^{2-} + 2h^+ \rightarrow S^0$  would consume holes and result in enhanced e-h separation. Once the S<sup>2-</sup> states at the surface were consumed the current might reach a steady state. Alternately, formation of S<sup>0</sup> on the surface could also result in a passivation effect that leads to current decay behavior.

Figure 4.16 (b) shows the potentiostatic current transient behavior of the TiO<sub>2</sub>-PbS QD composite electrode. This plot illustrates the stability of the TiO<sub>2</sub>-PbS QD system as a photo-anode. It was observed that the photocurrent density of the sample decreased continuously with time. This decrease had two components: 1) decrease in the total current, and 2) increase in the dark current. Both of these observations indicated that the TiO<sub>2</sub>-PbS QD composite was not stable.

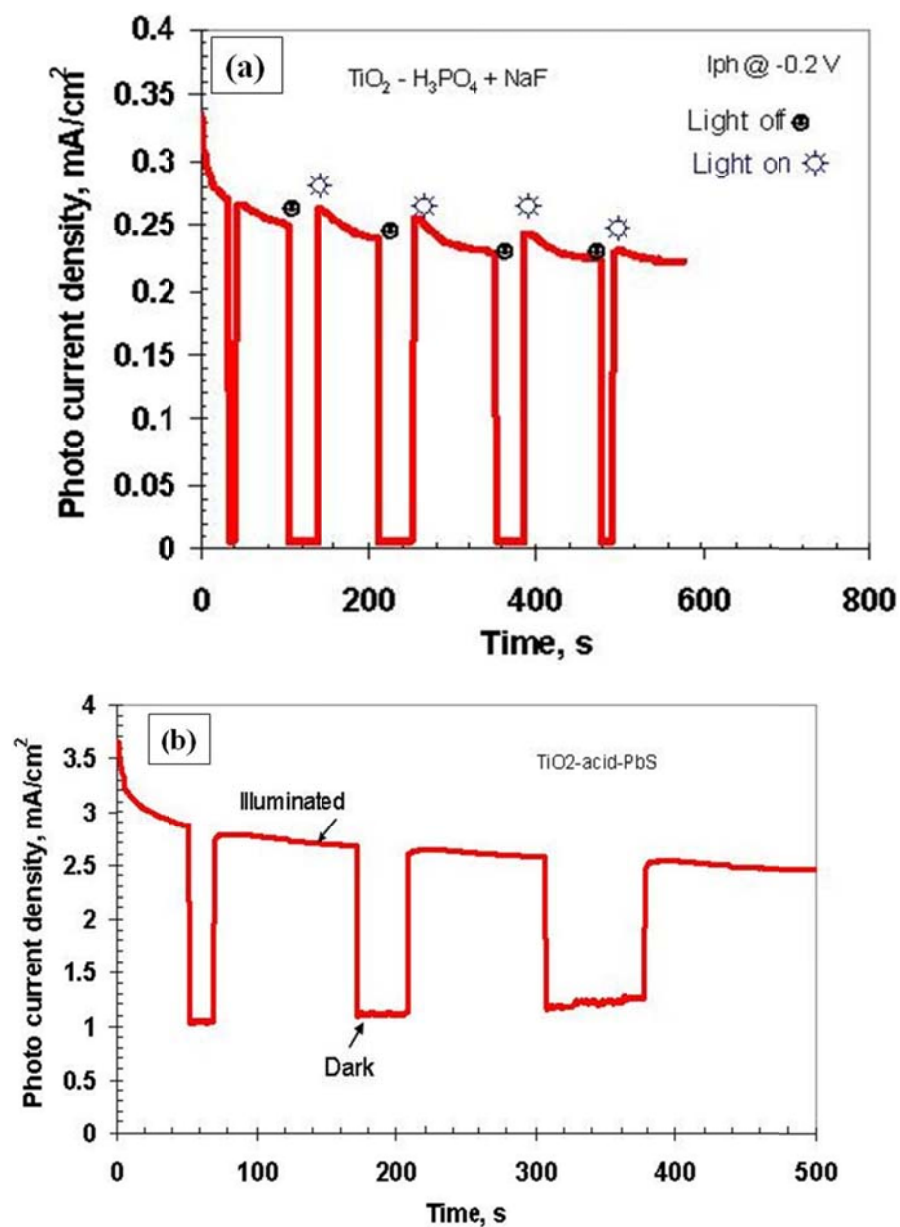


Figure 4.16: Long-term photocurrent stability (current vs time) study of the materials transient behavior of (a) acid anodized  $\text{TiO}_2$ ; and (b) prepared composite  $\text{TiO}_2\text{-PbS}$ . The photon source was applied by AM 1.5 light in polysulfide electrolyte

### 4.3.5 Mott-Schottky Study

The Mott-Schottky study was performed in order to observe the effect of light on the charge carrier density of the materials. These experiments were performed in the PEC cell described in section 3.4, and the results were plotted (Figure 4.17 and 4.18). The linear portion of the Mott-Schottky plot, charge carrier densities can be calculated using the relation,

$$N_D = \frac{2}{e\epsilon\epsilon_0 m}$$

Where,

$N_D$  = charge carrier density;  $e$  = elementary electron charge;  $\epsilon$  = dielectric constant and  $\epsilon_0$  = permittivity in vacuum;  $m$  = slope of the  $1/C^2$  versus potential  $P$

The prepared materials followed the plots as shown in Figures 4.17 and 4.18. The samples were preconditioned at an open circuit potential in the electrolyte before carrying out the Mott-Schottky experiments. The slope of the linear portion of the  $1/C^2$  Vs potential plot did not change upon illumination. The charge carrier concentrations calculated based on the slope of the linear portions were  $4.1 \times 10^{20}$  and  $4.3 \times 10^{20} \text{ cm}^{-3}$  for dark and illuminated conditions respectively.

Figure 4.17(a) shows the Mott-Schottky (M-S) plot of  $\text{TiO}_2$  nanotubes prepared in acid solution with and without the illuminated conditions. The increase in the  $1/C^2$  values with the increase in the potential towards the positive direction indicated that the  $\text{TiO}_2$  nanotubes showed an n-type conductivity. A slight increase in the charge carrier density was observed upon illumination. The flat band potential of this sample was calculated to

be  $-0.64$  V (Ag/AgCl). The charge carrier densities were  $4.1 \times 10^{20}$   $\text{cm}^{-3}$  and  $4.3 \times 10^{20}$   $\text{cm}^{-3}$  under dark and illuminated conditions, respectively.

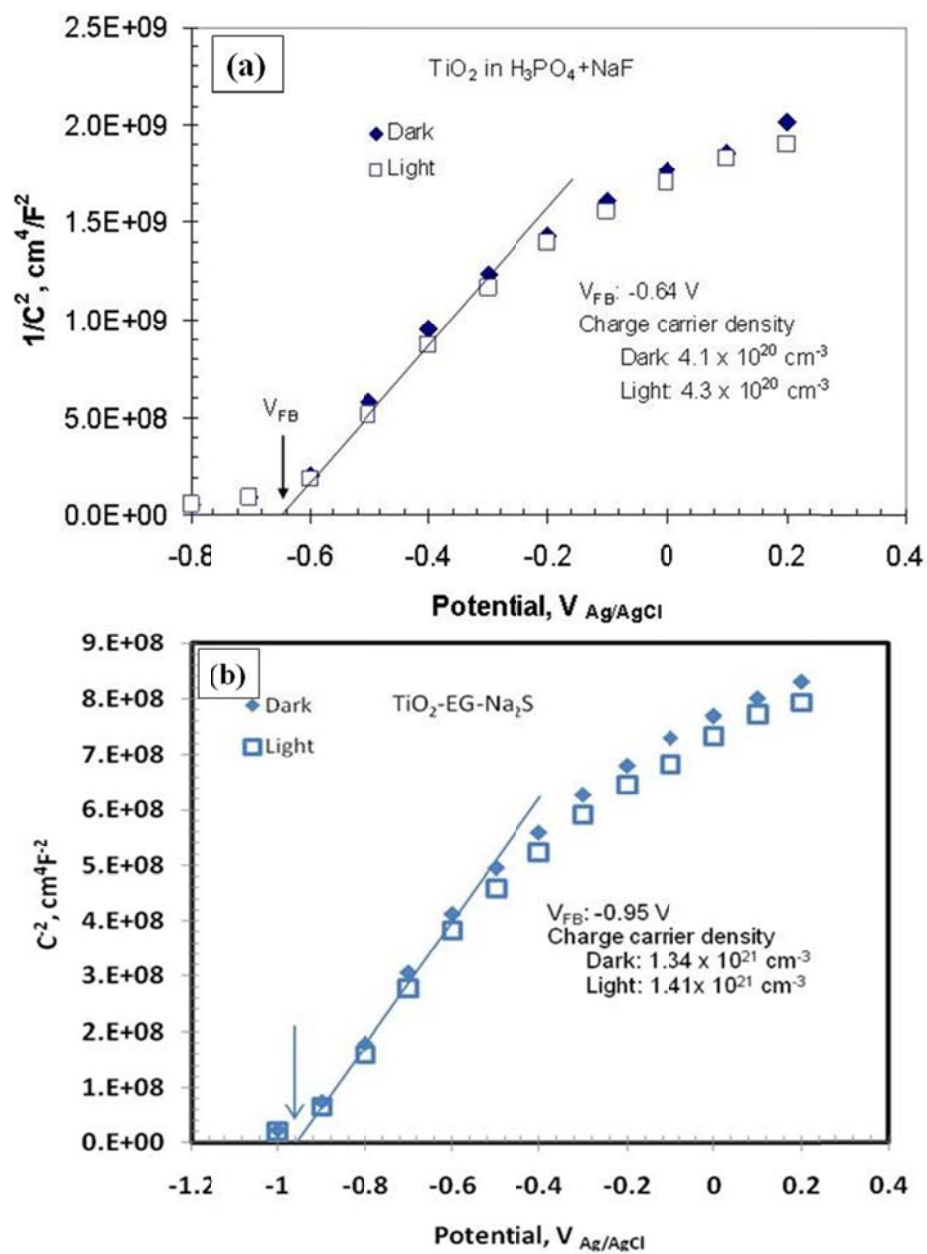


Figure 4.17: Mott-Schottky plots for the annealed TiO<sub>2</sub> samples with and without illumination: (a) Acid anodized sample; and (b) ethylene glycol anodized samples.

Figure 4.17(b) shows the M-S results of the TiO<sub>2</sub> nanotubes prepared in the ethylene glycol based solution. This sample showed higher charge density than the TiO<sub>2</sub> sample prepared in the 0.5 M H<sub>3</sub>PO<sub>4</sub> +0.5wt% NH<sub>4</sub>F solution. The flat band potential of the TiO<sub>2</sub> nanotubes prepared in the EG solution was more negative than that of TiO<sub>2</sub> prepared in acid solution. More negative flat band potential of n-type semiconductor will be advantageous for two reasons:

- 1) For electrochemical hydrogen generation applications a negative flat band potential with reference to H<sub>2</sub>/H<sub>2</sub>O energy level helps easy electron transfer for spontaneous hydrogen reduction
- 2) The larger the negative flat band potential the greater the band bending, when exposed to an electrolyte with a positive redox potential. This increases band bending will generate high photo potential.

The negative shift in the flat band potential could be attributed to the presence of high density surface states that act as electron traps. Anodization in ethylene glycol solution could introduce more oxygen vacancies that act as electron traps in the nanotubes as compared to the sample anodized in aqueous acid-fluoride solution. Since the charge carriers are associated with oxygen vacancies, higher charge carrier density of TiO<sub>2</sub>-EG sample also supports the correlation between oxygen vacancies and negative shift in the flatband potential.

Figure 4.18 (a) shows the M-S plot of PbS sensitized on the TiO<sub>2</sub> prepared using acidic solution (TiO<sub>2</sub>-PbS) composite electrode. Sensitization with PbS QDs shifted the flat band potential of the TiO<sub>2</sub> to a less negative value. No significant change in the

charge carrier density could be observed. The composite electrode showed an n-type semiconducting character indicating that the PbS QDs were essentially an n-type semiconductor. The flat band potential did not change upon light illumination. On the other hand, the  $\text{TiO}_2$  (EG)-PbS QD sample showed a complex behavior. There was an apparent increase in the charge carrier density as observed from the significant change in the slope of the M-S plot (Figure 4.18 (b)). Interestingly the flat band potential of the sample shifted to a less negative value upon illumination. This observation indicates that the holes are not consumed at an adequate rate at the electrode/electrolyte interface. Accumulation of the holes at the electrode surface could shift the flat band potential to a less negative or more positive value. Relatively lower charge carrier density of the  $\text{TiO}_2$  (EG)-PbS QD sample than that of  $\text{TiO}_2$  (acid)-PbS sample, and possible low coverage of PbS-QD on the nanotubes could be distributed to the hole accumulation.

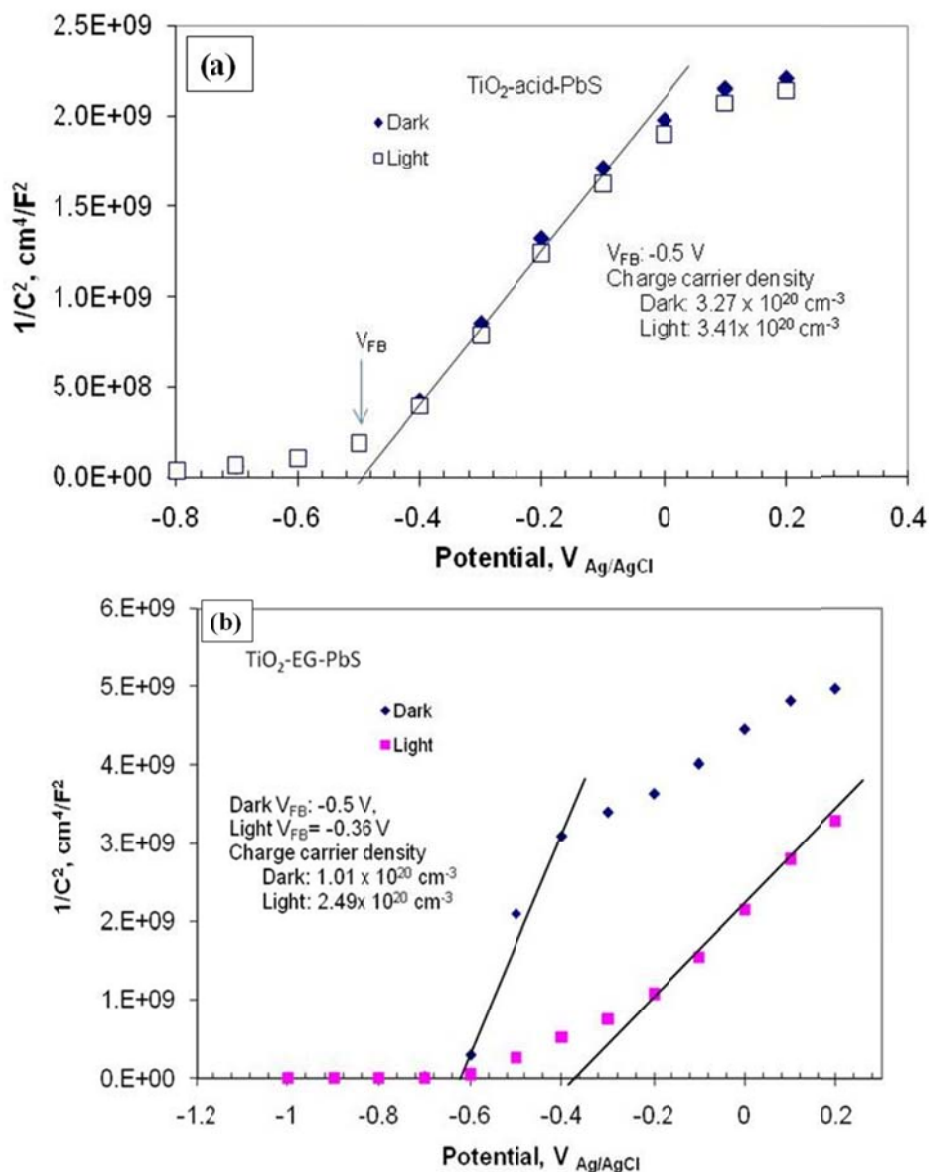


Figure 4.18: Mott-Schottky plots of the PbS-TiO<sub>2</sub> with and without illumination: (a) PbS sensitized in acid anodized TiO<sub>2</sub>; and (b) PbS sensitized in Ethylene Glycol anodized TiO<sub>2</sub>

Although the TiO<sub>2</sub> nanotubes did not show any change in the slope when no illumination was applied, the change was observed in the PbS sensitized TiO<sub>2</sub> anodized in Ethylene Glycol solution. The slope of the  $1/C^2$  vs Potential was decreased when the photoanode was illuminated. This indicates that there is an increase in carrier charge

concentration. After the calculation of the charge carrier concentrations based on the slope of the linear portions, the concentrations were  $1.01 \times 10^{20}$  and  $2.49 \times 10^{20} \text{ cm}^{-3}$  for dark and illuminated conditions, respectively.

#### 4.3.6 Electrochemical Impedance Analysis

An electrochemical impedance study helped to evaluate the electrode surface/electrolyte interface under dark and illuminated conditions. Figure 4.19 show the complex plane electrochemical impedance plots of our materials in the polysulfide electrolyte. The samples showed higher impedance without illumination. When illuminated the impedance decreased considerably because of the photo generated charge carriers. Application of external bias further decreased the impedance. It is interesting to note that the illumination significantly affected the imaginary component of the impedance. The real impedance component could be considered predominant by the charge transfer resistance and the imaginary impedance reflected predominantly (diffusion controlled) mass transfer. The resistance to diffusion of charge carriers was considerably reduced because of the increase in their concentration upon illumination. Application of external field further reduced the activation barrier for mass transport. The large reduction in the impedance upon application of bias potential indicated the significance of the electric field for charge separation under illuminated condition.

Figure 4.19 (a) shows the results of electrochemical impedance spectroscopy of the TiO<sub>2</sub> nanotubes prepared in acidic solution. The Nyquist plot (Real vs. Imaginary Impedance) showed a depressed semicircle with very low electrolyte resistance. The

charge transfer resistance can be deduced from the radius of the semicircle. It is observed that the impedance of the sample decreased considerably upon light illumination. This is attributed to the generation of excess charge carriers upon illumination. Figure 4.19 (b) shows the Nyquist plots of the  $\text{TiO}_2$  prepared in ethylene glycol solution. This sample showed higher impedance than  $\text{TiO}_2$  (acid) sample. The higher impedance, especially impedance related to diffusion limited condition at low frequencies, could be attributed to the increased length of the  $\text{TiO}_2$  nanotubes prepared in EG solution. When illuminated this diffusion controlled impedance decreased as seen in the Figure 4.19 (b).

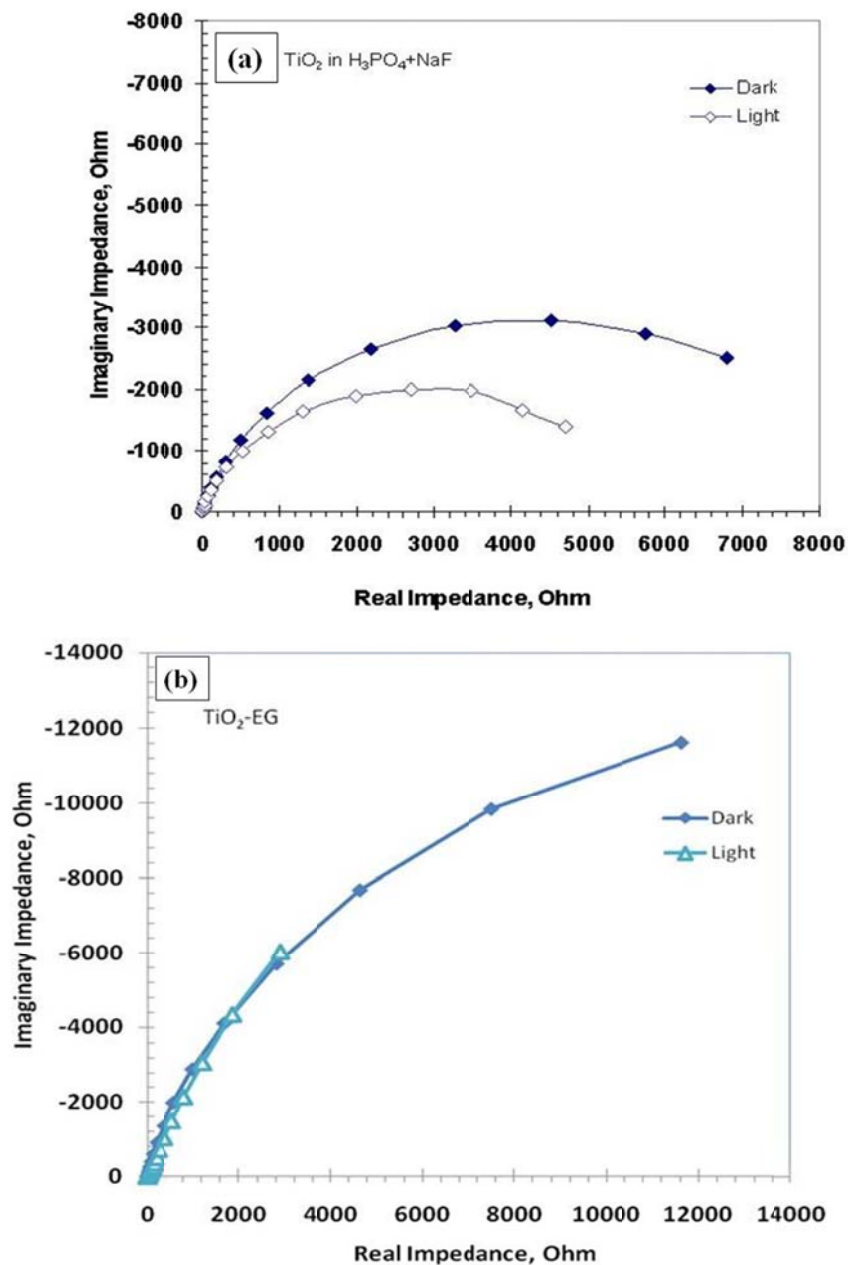


Figure 4.19: Complex plane electrochemical impedance behavior of the materials: a) TiO<sub>2</sub> prepared in acid solution and b) TiO<sub>2</sub> prepared in ethylene glycol based solution

Figure 4.20 shows the EIS results of the TiO<sub>2</sub> (acid) - PbS QD sample. A strongly suppressed semicircle type Nyquist plot could be observed for this sample indicating that the constant phase element of the equivalent RC (resistor-capacitor circuit) circuit of the electrochemical system was removed from the ideal one. The impedance of the sample

without illumination was high. Upon illumination the impedance decreased by almost an order of magnitude. The significant reduction in the impedance could be attributed to the multiple excitons generation within the QDs of PbS.

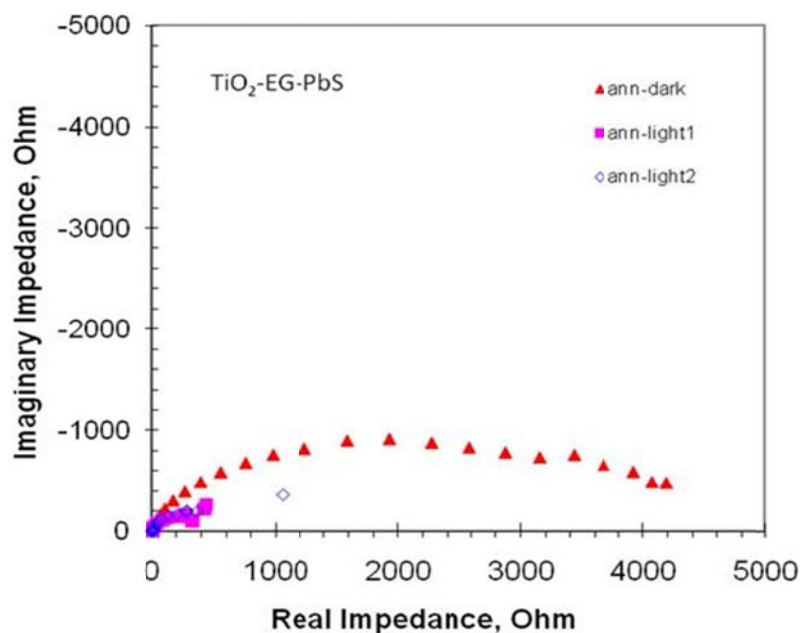


Figure 4.20: Complex plane electrochemical impedance behavior of the materials: PbS QDs sensitized  $\text{TiO}_2$  nanotubes

#### 4.3.7 Photovoltaic Study (PbS- $\text{TiO}_2$ )

The PbS quantum dots loaded  $\text{TiO}_2$  were used as the photo electrode and a thin Pt-coated ITO glass as the counter electrode for the photovoltaic cell. 0.2 M  $\text{Na}_2\text{S}_2\text{O}_3$  with 0.4 M  $\text{Na}_2\text{S}$  was used as the polysulfide electrolyte for the cell. The electrolyte is responsible for the charge separation generated by photons and flow of electrons in the circuit as the electrolyte follows the following regeneration reactions:

At the anode:



At the cathode:



According to the regeneration reactions stated above, we can conclude that the maximum photo potential generated by the polysulfide electrolyte system can be about 0.7 V, depending on the anodic reaction occurring at the PbS-TiO<sub>2</sub> surface. Figure 4.21 depicts the photovoltaic properties of the quantum dots sensitized nanotubes. The produced I-V plot of the PbS-TiO<sub>2</sub> as prepared under ultrasonic bath without the annealing showed the open circuit potential of about 0.28 V and short circuit potential of about 1.8 V. The fill factor was about 43%. The PbS prepared by maintaining the ionic stock solutions at the elevated temperature of 60<sup>0</sup>C and annealed at 300<sup>0</sup>C in an inert atmosphere for 30 minutes showed the improved photo potential of 0.34 V and a short circuit current density of 2.04 mA/cm<sup>2</sup> and the fill factor of 58%. The quantum dots sensitized deposited while passing the ultrasonic waves at room temperature and annealed the samples at 300<sup>0</sup>C in an inert atmosphere for 30 minutes showed the maximum fill factor of about 65.8%. The sample showed the open circuit potential of 0.4 V and short circuit current density of 2.6 mA/cm<sup>2</sup>. The results indicate that the reaction (1) mentioned above could be the anodic current flow path for the ultrasonicated samples.

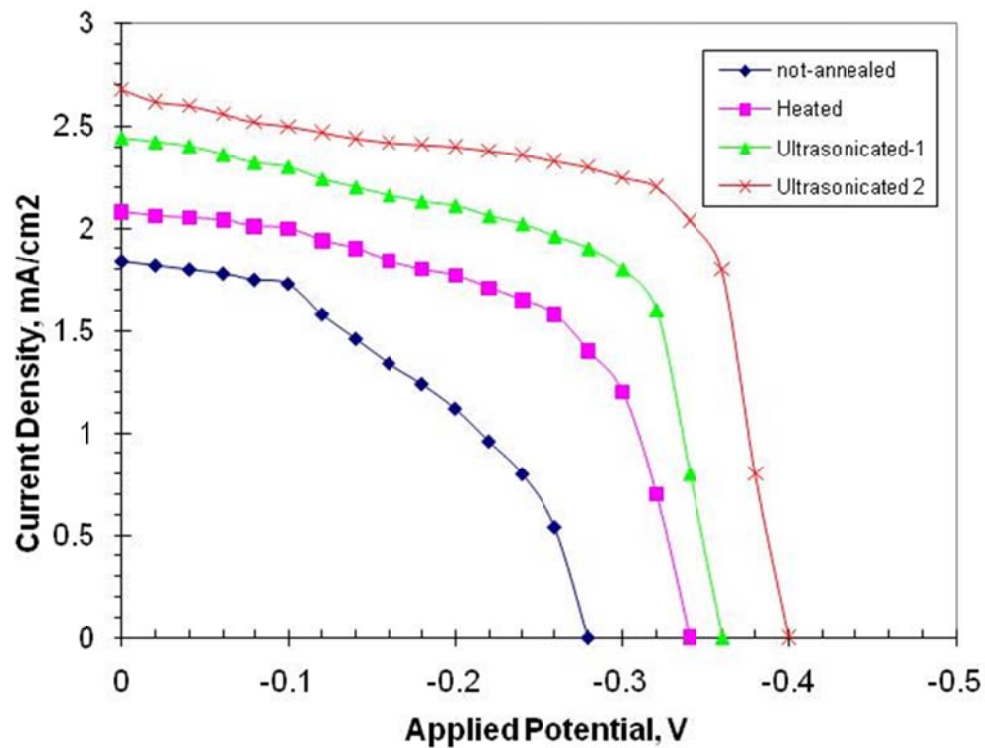


Figure 4.21: Characteristic of PbS-TiO<sub>2</sub> nanotubular photovoltaic cell with Na<sub>2</sub>S/Na<sub>2</sub>S<sub>2</sub>O<sub>3</sub> electrolyte system with illumination of simulated solar light

## Chapter 5: Conclusion

The photoelectrochemical and photovoltaic behavior of various nanostructured  $\text{TiO}_2$  and  $\text{PbS-TiO}_2$  composite samples was studied in the polysulfide electrolyte under simulated sunlight. The photo catalytic properties of  $\text{TiO}_2$  nanotubular samples prepared by anodization in ethylene glycol and acidic solutions were studied. Vertically standing, well organized  $\text{TiO}_2$  nanotube array obtained after anodization of the Ti metal, was uniformly deposited with PbS quantum dots. The quantum dots were successfully deposited using the SILAR technique. Various characterization studies were carried out to draw conclusion that the quantum dots of size ranging from 5 - 15 nm were uniformly deposited on the nanotubular structure with 60 - 70 nm diameter of the  $\text{TiO}_2$ . The composition ratio of Pb to S was also found as desired. The UV-vis results showed that the composite  $\text{PbS-TiO}_2$  absorbs in visible region with lower band gap of 1.65 eV. The approach led to design photocatalysts by filling 1D nanotube was a new direction in the field of multi-junction solar-cell materials. The process was strictly experimental; therefore a modelling approach should be adopted to understand the behavior of the quantum dots better. The appropriate computer model will help to understand the variability in the absorbance of the material by varying the material type and size of the quantum dots. In the future, the better fundamental studies of the interactions of quantum dots with nanotubes can show us the path for creating highly efficient PV system.

## References:

- [1] D. Y. Goswami and F. Krieth. (2007). *Energy Citation*.
- [2] M. A. Schilling and M. Esmundo, "Technology S-curves in renewable energy alternatives: Analysis and implications for industry and government," *Energy Policy*, vol. 37, 01/06/2009 2009.
- [3] I. E. Agency. (2004, 09/02). *World Energy Outlook*.
- [4] U. N. D. Programme. (2000, *United Nations Department of Economic and Social Affairs, and World Energy Council*. Available: <http://www.undp.org/seed/eap/activities/wea/>
- [5] N. Lewis. (2007, *Global Energy Perspective*. Available: <http://nsl.caltech.edu/energy>
- [6] Farlex, "The Free Dictionary," ed, 2010.
- [7] M. A. Green, *Third Generation Photovoltaics* Springer, 2003.
- [8] Available: <http://www.eere.energy.gov/>
- [9] E. Serrano, *et al.*, "Nanotechnology for sustainable energy," *Renewable and Sustainable Energy Reviews*, vol. 13, pp. 2373-2384, 2009.
- [10] B. G. Yogi, *Semiconductor Materials: An Introduction to Basic Principles*: Kluwer Academic/Plenum Publishers, 2003.
- [11] L. Solymar, *Electrical properties of Materials*, Seventh ed.: Oxford University Press, 2003.
- [12] H. O. Finklea, "Photoelectrochemistry: Introductory Concepts," *Photoelectrochemical Energy Conversion*, vol. 60, 1983.
- [13] T. Markvart, *Solar Electricity*: John Wiley & Sons, 1994.
- [14] J. L. Moll, *Physics of Semiconductors*. New York: McGraw-Hill, 1964.
- [15] S. J. Fonash, *Solar Cell Device Physics*: Academic Press, 1981.
- [16] O. S. Heavens, *Optical Properties of Thin Solid Films*. New York: Academic Press, 1955.
- [17] M. A. Green, *Solar Cells, Operating Principles, Technology and System Applications*: Prentice-Hall Inc, 1982.
- [18] D. F. Wang, *et al.*, "Tuning the Charge-Transfer Property of PbS-Quantum Dot/TiO<sub>2</sub>-Nanobelt Nanohybrids via Quantum Confinement," *Journal of Physical Chemistry Letters*, vol. 1, pp. 1030-1035, Apr 1 2010.
- [19] W. A. Tisdale, *et al.*, "Hot-Electron Transfer from Semiconductor Nanocrystals," *Science* vol. 328, pp. 1543-1547, 2010.
- [20] S. Sze, *Physics of Semiconductor Devices*. New York: Wiley & Sons, 1981.
- [21] R. T. Ross and A. J. Nozik, "Efficiency of Hot-Carrier Solar-Energy Converters," *Journal of Applied Physics*, vol. 53, pp. 3813-3818, 1982.
- [22] A. J. Nozik, "Spectroscopy and hot electron relaxation dynamics in semiconductor quantum wells and quantum dots," *Annual Review of Physical Chemistry*, vol. 52, pp. 193-231, 2001.
- [23] J. C. Phillips, *Bonds and Bands in Semiconductors*: Academic Press Inc.
- [24] T. M. Reith, "Aging effects in Si-doped Al Schottky Barrier Diodes," *Applied Physics Letters*, vol. 28, pp. 152-154, 1974.

- [25] B. V. Zeghbroek. (2007). *Principles of Semiconductor Devices*.
- [26] H. C. Pao, "Effects of Diffusion Current no Characteristics of Metal-Oxide (Insulator)-Semiconductor Transistors," *Solid-State Electronics*, vol. 9, pp. 927-937, 1966.
- [27] E. L. Wolf, *Princliplies of Electron Tunneling Spectroscopy*: Oford University Press, 1985.
- [28] M. A. Green, *et al.*, "Minority-Carrier Mis Tunnel-Diodes and Their Application to Electron-Voltaic and Photo-Voltaic Energy-Conversion .1. Theory," *Solid-State Electronics*, vol. 17, pp. 551-561, 1974.
- [29] J. Shewchun, *et al.*, "Minority-Carrier Mis Tunnel-Diodes and Their Application to Electron-Voltaic and Photo-Voltaic Energy-Conversion .2. Experiment," *Solid-State Electronics*, vol. 17, pp. 563-572, 1974.
- [30] Jeremy. (2000, *Quantum Mechanical Tunneling*. Available: <http://www.cord.edu/faculty/ulnessd/legacy/fall2000/hofferber/index.htm>
- [31] H. P. Maruska and A. K. Ghosh, "Photovoltaic Decomposition of Water at Semiconductor Electrodes," *Solar Energy Materials & Solar Cells*, vol. 23, pp. 129-139, 1978.
- [32] S. Kar, *et al.*, "Design and Operation of Electrochemical Solar-Cells," *Solar Energy*, vol. 23, pp. 129-139, 1979.
- [33] A. J. Nozik, "Electrode Materials for Photoelectrochemical Devices," *Journal of Crystal Growth*, vol. 39, pp. 200-209, 1977.
- [34] A. J. Nozik, "Nanoscience and Nanostructures for Photovoltaics and Solar Fuels," *Nano Letters*, vol. 10, pp. 2735-2741, Aug 2010.
- [35] A. J. Nozik, "Multiple exciton generation in semiconductor quantum dots," *Chemical Physics Letters*, vol. 457, pp. 3-11, May 20 2008.
- [36] A. Hagfeldt and M. Gratzel, "Molecular Photovoltaics," *Accounts of Chemical Research*, vol. 33, pp. 269-277, 2000.
- [37] *Photoelectrochemistry and Photovoltaics of Layered Semiconductors* vol. 14: Kluwer Academic Publishers, 1992.
- [38] U. o. Southampton. (1997, *Solar Electricity*. Available: <http://www.soton.ac.uk/~solar/intro/tech6.htm>
- [39] H. S. Rauschenbach, *Solar Cell Array Design Handbook : The Principles and Technology of Photovoltaic Energy Conversion*: Van Nostrand Reinhold Co, 1980.
- [40] F. Solar. (2009. Available: <http://investor.firstsolar.com/phoenix.zhtml?c=201491&p=irol-newsArticle&ID=1268014&highlight>
- [41] A. J. Nozik, "Quantum dot solar cells," *Physica E-Low-Dimensional Systems & Nanostructures*, vol. 14, pp. 115-120, Apr 2002.
- [42] B. Oregan and M. Gratzel, "A Low-Cost, High-Efficiency Solar-Cell Based on Dye-Sensitized Colloidal Tio<sub>2</sub> Films," *Nature*, vol. 353, pp. 737-740, Oct 24 1991.
- [43] B. Li, *et al.*, "Review of recent progress in solid-state dye-sensitized solar cells," *Solar Energy Materials & Solar Cells* vol. 90, pp. 549-573, 2006.

- [44] A. Hlinsch, *et al.*, "long-Term Stability of Dye-Sensitized Solar Cells," *Progress in Photovoltaics*, vol. 9, pp. 425-438, 2001.
- [45] P. Wang, "Stable 8% efficient nanocrystalline dye-sensitized solar cell based on an electrolyte of low volatility.," *Applied Physics Letters*, vol. 86, 2005.
- [46] C. Su, *et al.*, "Synthesis of heteroarchitectures of PbS nanostructures well-erected on electrospun TiO<sub>2</sub> nanofibers," *Journal of Colloid and Interface Science*, vol. 346, pp. 324-329, 2010.
- [47] C. B. Murray, *et al.*, "Synthesis and Characterization of Nearly Monodisperse CdE (E = S, Se, Te) Semiconductor Nanocrystallites," *Journal of American Chemical Society*, vol. 115, pp. 8706-8715, 1993.
- [48] R. Vogel, *et al.*, "Quantum-Sized PbS, CdS, Ag<sub>2</sub>S, Sb<sub>2</sub>S<sub>3</sub>, and Bi<sub>2</sub>S<sub>3</sub> Particles as Sensitizers for Various Nanoporous Wide-Bandgap Semiconductors," *The Journal of Physical Chemistry* vol. 98, 1994 1994.
- [49] K. Grieve, *et al.*, "Synthesis and electronic properties of semiconductor nanoparticles/quantum dots," *Current Opinion in Colloid and Interface Science* vol. 5, pp. 168-172, 2000.
- [50] A. J. Nozik, "Advanced Concepts for Photovoltaic Cells," in *National Center for Photovoltaics and Solar Program Review*, Denver, CO, 2003.
- [51] C. Kittel, *Introduction to Solid State Physics*, eight ed.: John Wiley & Sons, Inc, 2005.
- [52] U. o. T. a. Austin. (2010, 18 June 2010). Highly Efficient Solar Cells Could Result from Quantum Dot Research.
- [53] R. Plass, *et al.*, "Quantum Dot Sensitization of Organic-Inorganic Hybrid Solar Cells," *Journal of Physical Chemistry B*, vol. 106, pp. 7578-7580, 2002.
- [54] K. Derbyshire. Silicon Quantum Dots promise solar cell efficiency boost. *Electro IQ*.
- [55] W. Lee, *et al.*, "Effect of single-walled carbon nanotube in PbS/TiO<sub>2</sub> quantum dots-sensitized solar cells," *Materials Science and Engineering B*, vol. 156, pp. 48-51, 2009.
- [56] W. Lee, *et al.*, "Chemical bath deposition of CdS quantum dots on vertically aligned ZnO nanorods for quantum dots-sensitized solar cells," *Electrochemistry Communications* vol. 11, pp. 103-106, 2009.
- [57] W. A. Tisdale, *et al.*, "Hot-Electron Transfer from Semiconductor Nanocrystals," *Science*, vol. 328, pp. 1543-1547, 2010.
- [58] M. A. Hines and G. D. Scholes, "Colloidal PbS Nanocrystals with Size-Tunable Near-Infrared Emission: Observation of Post-Synthesis Self-Narrowing of the Particle Size," *Advance Materials*, vol. 15, pp. 1843-1849, 2003.
- [59] B. K. Ridley, *Quantum Processes in Semiconductors*. New York: Oxford University Press, 1982.
- [60] P. Sudhagar, *et al.*, "Self-assembled CdS quantum dots-sensitized TiO<sub>2</sub> nanospheroidal solar cells: Structural and charge transport analysis," *Electrochimica Acta*, vol. 55, pp. 113-117, Dec 15 2009.
- [61] S. Banerjee, *et al.*, "Synthesis of Coupled Semiconductor by filling 1D TiO<sub>2</sub> Nanotubes with CdS," *Chemical Mater*, vol. 20, pp. 6784-6791, 2008.

- [62] N. Vlachopoulos, *et al.*, "Very Efficient Visible-Light Energy Harvesting and Conversion by Spectral Sensitization of High Surface-Area Polycrystalline Titanium-Dioxide Films," *Journal of the American Chemical Society*, vol. 110, pp. 1216-1220, Feb 17 1988.
- [63] M. Anpo, *et al.*, "Photocatalytic Hydrogenation of CH<sub>4</sub>, C<sub>2</sub>H<sub>2</sub> with H<sub>2</sub>O on Small-Particle TiO<sub>2</sub>: Size Quantization Effects and Reaction Intermediates," *Journal of Physical Chemistry* vol. 91, pp. 4305-4310, 1987.
- [64] K. Wilke and H. D. Breuer, "The influence of transition metal doping on the physical and photocatalytic properties of titania," *Journal of Photochemistry and Photobiology a-Chemistry*, vol. 121, pp. 49-53, Feb 15 1999.
- [65] F. W. Wise, "Lead salt quantum dots: The limit of strong quantum confinement," *Accounts of Chemical Research*, vol. 33, pp. 773-780, Nov 2000.
- [66] I. Kang and F. W. Wise, "Electronic structure and optical properties of PbS and PbSe quantum dots," *Journal of the Optical Society of America B-Optical Physics*, vol. 14, pp. 1632-1646, Jul 1997.
- [67] K. S. Leschkies, *et al.*, "Photosensitization of ZnO Nanowires with CdSe Quantum Dots for Photovoltaic Devices," *Nano Letters*, vol. 7, pp. 1793-1796, 2007.
- [68] R. J. Ellingson, *et al.*, "Highly Efficient Multiple Exciton Generation in Colloidal PbSe and PbS Quantum Dots," *Nano Letters*, vol. 5, pp. 865-871, 2005.
- [69] P. J. Goodhew, *et al.*, *Electron Microscopy and Analysis* third ed. London: Taylor and Francis, 2001.
- [70] N. Serpone, *et al.*, "Size Effects on the Photophysical Properties of Colloidal Anatase TiO<sub>2</sub> Particles - Size Quantization or Direct Transitions in This Indirect Semiconductor," *Journal of Physical Chemistry*, vol. 99, pp. 16646-16654, Nov 9 1995.
- [71] N. Serpone, *et al.*, "Subnanosecond Relaxation Dynamics in TiO<sub>2</sub> Colloidal Sols (Particle Sizes R(P)=1.0-13.4 Nm) - Relevance to Heterogeneous Photocatalysis," *Journal of Physical Chemistry*, vol. 99, pp. 16655-16661, Nov 9 1995.
- [72] M. L. Roukes, *Understanding Nanotechnology*: Warner Books, 2001.
- [73] H. Lee, *et al.*, "PbS and CdS Quantum Dot-Sensitized Solid-State Solar Cells: "Old Concepts, New Results"," *Adv Funct Mater*, vol. 19, pp. 2735-2742, 2009.
- [74] Y. F. Nicolau, "Solution Deposition of Thin Solid Compound Films by a Successive Ionic-Layer Adsorption and Reaction Process," *Applied Surface Science*, vol. 22-3, pp. 1061-1074, 1985.
- [75] S. Nasrazadani, *et al.*, "Lead adsorption on magnetite at 200 degrees C," *Corrosion*, vol. 64, pp. 509-516, Jun 2008.
- [76] H. Tamura, *et al.*, "Incorporation of Impurity Metal Ions in Electrolytic Manganese Dioxide," *Journal of Electrochemical Society*, vol. 141, pp. 2035-2040, 1994.
- [77] J. Tang, *et al.*, "Quantum Dot Photovoltaics in the Extreme Quantum Confinement Regime: The Surface-Chemical Origins of Exceptional Air- and Light-Stability," *Acs Nano*, vol. 4, pp. 869-878, Feb 2010.
- [78] J. B. Sambur, *et al.*, "Multiple Exciton Collection in a Sensitized Photovoltaic System," *Science*, vol. 330, pp. 63-66, Oct 1 2010.